

DRAFT: Wake Analysis of an Aerodynamically Optimized Boxprop High Speed Propeller

Alexandre Capitao Patrao*, first author, corresponding author

Chalmers University of Technology
Department of Mechanics and Maritime Sciences
Gothenburg, SE-41296
Sweden
alexandre.capitao.patrao@gmail.com

Tomas Grönstedt, second author

Chalmers University of Technology
Department of Mechanics and Maritime Sciences
Gothenburg, SE-41296
Sweden
tomas.gronstedt@chalmers.se

Anders Lundbladh, third author

GKN Aerospace Sweden & Chalmers University of Technology
Trollhättan, SE-46181
Sweden
anders.lundbladh@gknaerospace.com

Gonzalo Montero Villar, fourth author

Chalmers University of Technology
Department of Mechanics and Maritime Sciences
Gothenburg, SE-41296
Sweden
villar@chalmers.se

Keywords:

Declaration of interest: None.

ABSTRACT

The Boxprop is a novel, double-bladed, tip-joined propeller for high-speed flight. The concept draws inspiration from the box wing concept and could potentially decrease tip vortex strength compared to conventional propeller blades.

Early Boxprop designs experienced significant amounts of blade interference. By performing a wake analysis and quantifying the various losses of the flow it could be seen that these Boxprop designs produced 45% more swirl than a conventional reference blade. The reason for this was the proximity of the Boxprop blade halves to each other, which prevented the Boxprop from achieving the required aerodynamic loading on the outer parts of the blade.

This paper presents an aerodynamic optimization of a 6-bladed Boxprop aiming at maximizing efficiency and thrust at cruise. A geometric parametrization has been adopted which decreases interference by allowing the blade halves to be swept in opposite directions. Compared with an earlier equal-thrust Boxprop design the optimized design features a 7% percentage point increase in propeller efficiency and a lower amount of swirl and entropy generation. A vortex-like structure has also appeared downstream of the optimized Boxprop, but with two key differences relative to conventional propellers. 1) Its formation differs from a traditional tip vortex and 2) it is 46% weaker than the tip vortex of an optimized 12-bladed conventional propeller.

1 INTRODUCTION

The open rotor has been the subject of intense research during the last decade because of its advantage in fuel efficiency relative to turbofan engines. The predicted double-digit savings in fuel consumption [1] compared to modern turbofans are reached by employing two unducted counter-rotating propellers blades, thereby increasing the bypass ratio of the engine. The removal of the shroud around the propellers decreases aerodynamic drag, but unfortunately it also removes the ability to shield the surroundings from the noise produced by the two counter-rotating propeller rows.

While the potential decrease in fuel consumption of the Counter-Rotating Open Rotor (CROR) seems very promising, the noise levels are higher than for turbofan engines. One of the main sources of noise for the open rotor is the impingement of the front rotor tip vortices onto the rear blades, a noise source which in modern designs has been mitigated by clipping the rear rotor. The existence of a tip vortex therefore affects the aerodynamic performance in two ways: 1) The front rotor tip vortex is an aerodynamic loss, which lowers efficiency for the entire open rotor 2) clipping of the rear rotor yields a shorter blade with increased aerodynamic loading, and an inability to cancel out swirl emanating from the tip region of the front rotor.

An alternative route for noise mitigation might lie in radically different propeller shapes and configurations such as the Boxprop high speed propeller. This propeller type is composed of blade-pairs joined at the tips, forming a blade arc as shown in Fig. 1, where the first propeller row in the CROR is composed of Boxprop blades. The blade halves that make up the Boxprop are named Leading Blade (LB) and Trailing Blade (TB) relative to the direction of rotation, as shown in Fig. 2. The joined blade tips are the key design feature of the Boxprop, and earlier studies have shown that it is possible for a Boxprop to operate without producing a traditional, near-circular tip vortex [2], as is found in conventional propeller blades. If the Boxprop would then be used as the front rotor of a CROR, then a lack of or weakened tip-vortex could provide acoustic benefits relative to conventional blades.

In order to analyze the benefits, challenges, and possible design changes for propellers in general and the Boxprop in particular, a wake analysis method was developed in a previous paper by the authors [3]. This analysis method enables a systematic breakdown of the various losses in the flow around a propeller and the ability to distinguish and quantify the strength of tip vortices and blade wake velocity deficits. This breakdown provides loss estimates in terms for propeller shaft power for swirl, radial flow, tip vortex flow, and irreversibilities arising from entropy creation. The magnitudes of these losses can then be compared for different propeller designs. This method was applied on a Boxprop design at cruise conditions (Mach 0.75, 10 668 m altitude) and showed that it suffered from higher amounts of swirl relative to equal-thrust conventional propellers. For a CROR, residual swirl from the front propeller could be recuperated in the rear counter-rotating propeller, but for a single propeller it is a loss and should therefore be minimized. For the Boxprop design the large amount of swirl stemmed from interference between the blade halves, which decreased the amount of lift and thrust which could be produced between mid-span and the tip of the blade. This forced the blade designs to produce more thrust closer to the hub, resulting in higher amounts of swirl. In order to decrease interference between the Boxprop blade halves, two counter-measures were suggested:

1. Sweeping the blade halves in opposite directions. As is shown in Fig. 3, the trailing and leading blades could be moved upstream and downstream along the flow direction, respectively, decreasing blade interference.
2. Increasing the distance in the tangential direction between the blade halves as shown in Fig. 3, thereby allowing the pressure and suction sides of the blade halves to propagate more freely in space.

Existing propeller design methods such as the Blade Element Momentum [4], Vortex [5], and lifting line methods [6] are not directly applicable on the Boxprop. Early Boxprop work [7] showed that the Boxprop required different camber and angle-of-attack distributions for each blade half due to the interference between them, and this could not be accounted for by using the BEM/Vortex methods. The flow around the Boxprop is also transonic, and can feature shocks in the blade passage, thereby invalidating the use of lifting line methods, which have otherwise been used successfully for the design of conventional open rotor blades [6]. As a consequence, the chosen path for finding aerodynamically optimal Boxprop designs was to employ the use of 3D CFD together with an evolutionary algorithm ([8], [9] and [10]), an approach which has been used successfully in the optimization of CROR designs ([11], [12]). The newly developed wake analysis method is then used to analyze the resulting designs.

The contribution of this paper is in the form of results and conclusions from the aerodynamic optimization of a novel, 6-bladed, Boxprop high speed propeller. A blade geometry parametrization is presented which enables the Boxprop blade to explore design variations for decreasing blade interference and aerodynamic losses. Substantial performance improvements relative to a previously published (legacy) [3] design is demonstrated. It will be shown that for the novel Boxprop concept one distinct geometric feature, the chord displacement angle κ , is largely responsible for decreasing blade interference. The magnitude of the losses in the flow as well as the wake structures will be compared to two optimized, conventional, equal-thrust propellers equipped with 6 and 12 blades, highlighting the differences in performance and flowfield between the two different propeller types.

2 METHODOLOGY

2.1 Optimization framework

The structure of the multi-objective optimization platform employed in this paper is shown in Fig. 4 and is described in greater detail in [13]. The objective functions of the optimization were to maximize the propeller efficiency and thrust coefficient of the Boxprop at cruise conditions, which for this paper corresponds to Mach 0.75 and a flight altitude of 10 668 m at ISA conditions [14]. The optimization variables were divided into two main categories; variables which were used to construct the blade stacking line, and variables that were used to set airfoil sectional properties such as camber, chord, and angle-of-attack relative to the undisturbed flow.

The blade stacking line was constructed using Bézier curves, as is illustrated in Fig. 5. The control points P_i used for constructing the stacking line Bézier curve are in turn defined using a blade passage distance d_i and a chord displacement angle κ_i , which were used as optimization variables. The chord displacement angle κ_i and passage distance d_i effectively controls how much the LB and TB are swept. These two parameters together with the radial positions for P_1 (hub radius, fixed), P_2 (set as an optimization variable), P_3 (set as identical to the tip radius, fixed) and P_4 (tip radius, fixed) fully define the stacking line Bézier curve. Using this approach, the LB and TB become mirror-symmetric, which enables each blade half to be swept in opposite directions, while providing a balanced mechanical layout whose center-of-gravity lies close to the z-axis of the rotor. The sectional properties of the propeller were also defined as radial distributions by means of Bézier curves, whose control points were used as design parameters for the optimization, as is shown for camber in Fig. 6. Once the sectional properties camber, chord, and angle-of-attack were set, NACA16 airfoil profiles were constructed, positioned on planes normal to the stacking line, and rotated to meet the undisturbed flow at the specified angle-of-attack. For this optimization effort, computational cost was reduced by setting a fixed airfoil section thickness t/c distribution identical to the one used by the NASA SR7L propeller [15]. The SR7L high speed propeller also employed NACA16 airfoil sections and operated at similar transonic flow conditions. The abundance in design data pertaining to the SR7L made it a suitable source of information for setting up realistic thickness, chord, and camber distributions, especially since this propeller was ultimately manufactured and tested in a wind tunnel at transonic conditions. In total 32 parameters define a Boxprop design using the parametrization in this paper, and were used as optimization variables.

The optimization process starts by creating an initial design set by performing a Latin Hypercube Sampling (LHS) of the design space. The number of samples required was calculated using Eq. (1) by assuming that the topology of the objective function $f(\chi_1, \chi_2, \dots, \chi_n)$ response surface is similar to the n-dimensional quadratic polynomial given in Eq. (2). For this paper $n = 32$ was used for the Boxpop, which amounts to a LHS sampling size of 561 samples.

$$N_{points} = \frac{(n_{dim} + 1)(n_{dim} + 2)}{2} \quad (1)$$

$$f(\chi_1, \chi_2, \dots, \chi_{n_{dim}}) = \sum_{i,j=1}^{n_{dim}} [A_{ij}\chi_i\chi_j + B_i\chi_i] + C \quad (2)$$

The meshing software ICEM CFD was then used to create a structured hexahedral mesh for each of the 561 samples of the initial design set, whose meshes were then pre-processed using ANSYS CFX. The simulation domain for the optimization cases consists of an inner 3D domain solved in the rotating frame-of-reference, representing a single blade passage. The domain also includes an outer quasi-2D domain solved in the stationary frame-of-reference, and is shown in Fig. 7. This domain setup allows the pressure field of the propeller to propagate outwards while maintaining a low overall mesh cell count, which is important for being able to run the hundreds of CFD cases necessary for the optimization. A study of the domain size and mesh count effect on performance has been published in a previous paper by the authors [13], and the same domain dimensions were used here. The mesh used in this paper was a modified variant of the one chosen in that paper, and features an increased cell count in the tangential direction of the domain in order to better capture the shocks on the suction side of the blade halves, resulting in a total mesh cell count of 1.84 million. The meshes also adhere to an average first node height of $y_{ave}^+ < 2$ normal to the blade surfaces, as was recommended by the solver [16]. In order to save computational resources the nacelle was modelled as a cylindrical surface with a free-slip boundary condition. Previous work by the authors [3] has shown small differences in performance values using this simplification, which compared the obtained values in thrust and propeller efficiency for cases with no-slip and free-slip boundary conditions for the propeller hubs. This comparison yielded a proportional difference of +2.05% for the thrust coefficient and an absolute difference of -0.76% in propeller efficiency for the Boxprop versus a no-slip case. Corresponding values for an analyzed conventional propeller were +1.27% for the thrust coefficient and -0.17% lower propeller efficiency.

The solver ANSYS CFX was used for simulating the steady-state performance of each design in the initial design set, solving the compressible flow equations (RANS) together with the $k - \omega$ SST turbulence model. The inner 3D domain and the outer 2D domain were connected using frozen rotor interfaces (see Fig. 7) since they were solved in a rotating and a stationary reference frame, respectively. The Inlet boundary conditions were set by specifying total pressure, total temperature, flow direction, and a turbulence intensity of 1%. The Opening boundary uses the CFX equivalent of a free-stream boundary condition (opening/entrainment boundary condition) with specified static pressure and a zero-gradient turbulence boundary condition. The Outlet boundary uses a static pressure boundary condition, set as the ISA atmospheric pressure at an altitude of 10665 m. Both the inner 3D domain and the outer 2D domain employ rotational periodicity, and the blade surfaces were set as no-slip surfaces.

At this stage in the optimization framework a meta-model was constructed to be used by the Genetic Algorithm (GA). Since this optimization algorithm is stochastic it requires a large amount of objective function evaluations, in this case the Boxprop propeller efficiency and thrust. Using CFD for evaluating the objective functions would be prohibitively expensive, so a Radial Basis Function (RBF) type meta-model was constructed from the existing CFD results, and the objective function evaluations needed by the GA were performed (estimated) by the RBF. Details on the implementation and use of the RBF are given in [13].

The GA employed in this paper is based on the NSGA-II multi-objective evolutionary algorithm [17] and its components and layout are shown in Fig. 8. The GA creates an initial population popP of Boxprop designs and evaluates their objective functions using the RBF. The individual designs of the population popP were then ranked and put through the tournament selection,

crossover, and mutation processes of the NSGA-II algorithm. This results in a new population popQ of Boxprop designs, whose objective functions were then evaluated using the RBF. The last evolutionary process which the GA undergoes was the elitism process, which was carried out by combining popP and popQ into a new population popPQ. This aggregated population was then ranked and sorted, and a new population popP was created by taking the highest ranking individuals from the population popPQ. In this way, the best designs of each generation in the GA are preserved, and the globally optimal designs are never lost. In this paper, the GA operates for 100 generations before selecting a number of designs for evaluation using CFD. The selected designs were then meshed, simulated with ANSYS CFX, post-processed, their data added to the meta-model, and the GA-process starts once again. For this paper, this outer loop continued until no improvement was found in the maximum propeller efficiency and thrust coefficient for the entire population in the last 300 CFD evaluations.

2.2 The wake analysis method

Selected propeller designs from the optimization effort will be re-simulated with finer meshes and analyzed in more detail using the wake analysis developed by the authors [3]. This analysis method provides a systematic breakdown of the work added by the propeller (shaft power) to the flow into entropy lost work, reversible pressure changes, and kinetic and turbulent energy changes. The magnitude of these terms provide insight into how much of the work added by the propeller is beneficial for propulsion, recoverable in a downstream rotor, or pure losses. A velocity decomposition is also introduced which clearly distinguishes the tip vortices and wakes from the mean flow, which is then used for estimating the strength of these flow features in terms of shaft power. The full detailed derivation is available in [3], and is briefly recapped here. For a control volume enclosing the propeller blade (see Fig. 9) there are three surfaces. Surface 1 is located far upstream of the propeller and has uniform properties equal to their freestream values. Surface S is defined as a streamsurface with no mass flux across it, and Surface 2 is located downstream of the propeller and its flow properties are not uniform. With the two conditions imposed on Surface 1 and Surface S, a control volume analysis yields that the shaft power input into the control volume equals the mass flow integral of the total enthalpy change on surface 2:

$$P_{shaft} = \int_2 \Delta h_0 d\dot{m} = \int_2 (h_{02} - h_{01}) d\dot{m} \quad (3)$$

Here the change in total enthalpy denotes the change between positions on plane 2 and the constant freestream properties, which is denoted as h_{01} . Constructing a control volume with surface 1 far upstream with uniform flow properties and surface S as a streamsurface reduces the entire control volume analysis to only a surface integral evaluated on surface 2. The change in total enthalpy in the control volume is accounted for by calculating the change in total enthalpy $\Delta h_0 = h_{02} - h_{01}$, where index 1 denotes the freestream values. An identical expression to equation (3) is obtained if one follows a streamline for an elemental fluid particle travelling from a surface far upstream (1) to a surface downstream of the rotor (2), as is illustrated in Fig. 9 and shown in Eq. (4).

$$d\dot{W} = (h_{02} - h_{01})d\dot{m}$$

$$\text{Hence: } P_{shaft} = \int_2 d\dot{W} = \int_2 \Delta h_0 d\dot{m} = \int_2 (h_{02} - h_{01})d\dot{m} \quad (4)$$

The change in total enthalpy can be expanded into its constituents as is shown in Eq. (6), and can be expanded further into an irreversible entropy lost work term ϕ_s and a reversible pressure work term ϕ_p using the Gibbs relation in Eq. (5).

$$dh = Tds + vdp$$

$$\rightarrow \Delta h = h_2 - h_1 = \underbrace{\int_1^2 T ds}_{\phi_s} + \underbrace{\int_1^2 v dp}_{\phi_p} \quad (5)$$

$$\rightarrow \Delta h_0 = \underbrace{(\phi_s + \phi_p)}_{\Delta h} + \Delta \left(\frac{1}{2} u_i u_i \right) + \Delta k \quad (6)$$

The entropy lost work term ϕ_s is evaluated using the approach used by Hall [18], Denton [19], Dixon [20], and Miller [21], while the pressure work term ϕ_p is obtained by subtracting the entropy lost work term from static enthalpy change:

$$\phi_s = \int_1^2 T ds \approx T_\infty (s_2 - s_1) \quad (7)$$

$$\phi_p = \int_1^2 v dp \approx (h_2 - h_1) - T_\infty (s_2 - s_1) \quad (8)$$

The kinetic energy term in Eq. (6) should be expanded to include the axial, radial, and swirl velocities:

$$\Delta \left(\frac{1}{2} u_i u_i \right) = \Delta \left(\frac{1}{2} (u_x^2 + u_r^2 + u_\theta^2) \right) \quad (9)$$

The changes in kinetic energy can be written as the differences between the downstream values (2) and the upstream values (1), assuming that no radial and swirl velocities exist in the freestream:

$$\Delta \left(\frac{1}{2} u_i u_i \right) = u_{x,1} \Delta u_x + \frac{1}{2} ((\Delta u_x)^2 + u_{r,2}^2 + u_{\theta,2}^2) \quad (10)$$

$$\Delta u_x = u_{x,2} - u_{x,1}$$

Including all the expressions for entropy lost work, pressure work, and kinetic energies results in the following equation:

$$P_{shaft} = \int_2 \left[\phi_s + \phi_p + u_{x,1} \Delta u_x + \frac{1}{2} ((\Delta u_x)^2 + u_{r,2}^2 + u_{\theta,2}^2) + (k_2 - k_1) \right] d\dot{m} \quad (11)$$

The final step is to include a velocity decomposition which distinguishes the tip vortex and blade wakes from the mean velocity field.

Therefore, the velocity components $u_i(r, \theta)$ are decomposed into a *circumferentially averaged velocity* $U_i(r)$ and an associated *perturbation* $v_i(r, \theta)$:

$$u_i(r, \theta) = U_i(r) + v_i(r, \theta) \quad (12)$$

$$U_i = \frac{1}{\Lambda} \int_0^{2\pi} \rho_2 u_n u_i d\theta \quad \Lambda = \int_0^{2\pi} \rho_2 u_n d\theta \quad (13)$$

Including these terms in Eq. (11) yields:

$$P_{shaft} = \int_A \rho_2 u_n \left[\phi_s + \phi_p + u_{x,1} \Delta u_x + \frac{1}{2} ((\Delta U_x)^2 + U_{r,2}^2 + U_{\theta,2}^2) + \frac{1}{2} ((\Delta v_x)^2 + v_{r,2}^2 + v_{\theta,2}^2) + (k_2 - k_1) \right] dA \quad (14)$$

The terms ϕ_p and $u_{x,1} \Delta u_x$ constitute the propulsive power, $U_{\theta,2}^2/2$ represents the recoverable kinetic energy, and the rest of the terms in Eq. (14) constitute losses. An explanation of the physical nature of each term is provided below:

- The entropy lost work term ϕ_s is a thermodynamic loss and increases when the flow experiences shocks, mixing, and viscous losses in boundary layers and shear layers.
- Thrust is represented by the pressure work term ϕ_p and axial momentum change $u_{x,1} \Delta u_x$. For a fully expanded jet slipstream the axial momentum change fully accounts for the produced thrust and propulsive power, but in proximity to the blade the pressure is not yet the same as in the freestream, and therefore the pressure work terms needs to be included. The pressure term ϕ_p increases when the flow passes through the propeller disk and decreases downstream, while the axial momentum experiences a corresponding increase. This is in accordance with simpler propeller theories such as the Actuator Disk Theory.
- The term $(\Delta U_x)^2/2$ represents the excess axial kinetic energy found in the jet downstream of the rotor. The mean radial $(\Delta U_r)^2/2$ kinetic energy is also a loss while the swirl $(\Delta U_\theta)^2/2$ kinetic energy could be recovered in a downstream stator or counter-rotating propeller.
- The kinetic energy bounded to the perturbations of the flow $((\Delta v_x)^2 + v_{r,2}^2 + v_{\theta,2}^2)/2$ – in this case propeller wakes and tip vortices – is a pure loss.
- The change in turbulent kinetic energy $(k_2 - k_1)$ occurs mostly in the boundary and shear layers in the flow. Eventually this term dissipates and is converted into entropy lost work. This term has been shown to be quite small [2], <0.5% of shaft power, and will be omitted from the rest of the analysis.

As mentioned earlier, selected propeller designs from the optimization effort will be analyzed with the wake analysis theory and compared to a legacy Boxprop design, highlighting which losses have been decreased in the new optimized designs. The simulation setup of the selected cases differs relative to the optimization cases in two ways:

- 1 The inner 3D domain is extended further out radially and axially compared to the optimization cases in order to better capture the development of the wake structures. This domain setup is illustrated in Fig. 10.
- 2 The mesh required for wake analysis needs to be significantly finer than the one needed for the optimization in order to avoid the artificial dissipation of sharp flow features such as wakes and vortices. A mesh study was performed with mesh sizes ranging from 9.9 to 48.9 million cells, with the coarsest mesh shown in Fig. 11. Convergence for the wake analysis terms was reached by evaluating the terms in Eq. (11) for five different meshes. The maximum absolute difference in the integrals of the terms were 0.65% of shaft power between the two finest meshes. The final mesh size used for the wake analysis simulations contained 48.9 million cells.

It is important to note the effect of the integration surface size on the terms of the wake analysis. A small radius (see Fig. 10) for the integration surface could possibly miss important flow features, while a large radius makes the surface come close to the frozen rotor interfaces which should be avoided. In order to investigate the effect of this, four different integration surface radii were used to compute the change in total enthalpy and the various terms in Eq. (11) (excluding the turbulent kinetic energy). The differences in the wake analysis terms for each surface are shown in Table 1, where the difference versus the largest surface has been used. As can be seen, the difference in total enthalpy change is very small between the analyzed planes, with a change of -0.09% of engine shaft power between the smallest and largest plane. For ϕ_p the value changes with -8.70% of shaft power for the smallest relative to the largest surface, while for the axial momentum term $u_{x,1}\Delta u_x$ this behavior can be seen to act in the opposite direction, so that the axial kinetic term changes with +9.19% of engine shaft power from the smallest to the largest plane. This is expected since the pressure field from the propeller extends quite far out from the propeller. The size of the integration surface seems to affect the relative amount of shaft power input into either ϕ_p or $u_{x,1}\Delta u_x$, but their sum which constitutes the propulsive power stays relatively constant with respect to integration surface size. The loss terms which are to be compared in this paper, namely entropy lost work ϕ_s , excess axial kinetic energy $(\Delta u_x^2)/2$, radial kinetic energy $u_r^2/2$, and swirl kinetic $u_\theta^2/2$ energy differ only by less than 0.25%. In conclusion, it is critical to use identical integration surface sizes in order make a fair comparison between two different propeller types. This conclusion was also reached in collaboration with Andersson [22] when adapting a similar wake analysis for naval propellers in open water. For the rest of this paper an integration surface size of $1.8R$ is used, as has been shown earlier in Fig. 10, which places the outer radius of the integration surface one blade height away from the frozen rotor interface.

The wake analysis is performed on one selected design with ID name BP1112 from the optimization effort, seen in Fig. 12. The wake analysis is carried out using an in-house Matlab code which reads data exported by ANSYS CFX for a number of downstream planes. These planes correspond to surface 2 in Fig. 9 for different downstream positions from the Boxprop blade. In this way it is possible to investigate how the trends of the different terms of the wake analysis method vary with downstream distance.

3 RESULTS

Early optimization results for maximizing propeller efficiency and thrust for a 5-bladed Boxprop have been published for a limited amount of design variables [13], and showed a modest improvement in efficiency. The focus of that study was on the development of the optimization framework, and therefore the optimization variables only affected the angle-of-attack distributions and the stacking line. Onwards from that study additional design parameters such as camber and chord distributions have been included in order to increase the propeller efficiency as much as possible for optimized designs. The operating condition and propeller properties used in the optimization are shown in Table 2, and the number of blades for this Boxprop optimization has been chosen to match the number of front rotor blades on published modern open rotor geometries [18, 23, 24, 6], which commonly feature 11-12 front rotor blades. Since the Boxprop is composed of two blade halves the choice of 6 Boxprop blades is seen as an appropriate choice. Table 2 also shows ranges for chord, camber, and thickness at root and tip. Note that the ranges for the chord displacement angles κ_i are strictly positive since previous optimization attempts [13] revealed that the majority of Boxprop designs showed this tendency. This choice of ranges will be further supported later in this paper.

The overall number of designs analyzed with CFD in the optimization effort amounted to 1452 individual designs. The Pareto front of this population is shown in Fig. 12, where the propeller efficiency of all designs has been subtracted by the propeller efficiency of a 5-bladed scaled up (diameter 0.75 m to 4.2672 m) legacy Boxprop design GPX701 [7], and shows that an improvement of approximately 7% has been achieved by design BP1112 for the thrust coefficient of $C_T = 0.486$. This increase in efficiency has been calculated after re-simulating the BP1112 design with a finer mesh (48.9M cells) equivalent to the one used to simulate the legacy GPX701 Boxprop. Even larger increases in efficiency can be seen, but these are for propellers with lower aerodynamic loading than the GPX701.

The legacy Boxprop GPX701 featured blade halves that were quite close to each other, as is visible in Fig. 2. The proximity of the two blades led to blade interference, which is manifested by a high Mach number flow in the blade passage between the leading and trailing blade (as is shown in Fig. 13a), thereby decreasing the aerodynamic loading on the trailing blade and the amount of generated thrust. For an equal-thrust blade, this means that more thrust is generated close to the propeller hub, thus generating more swirl and leading to lower propeller efficiency. For all the optimized designs along the Pareto front shown in Fig. 12 one geometric feature has been instrumental in decreasing blade interference, namely the forward-sweeping (upstream) the TB and rearward-sweeping (downstream) of the LB. This feature is present in all optimal designs, and is illustrated in Fig. 14. Here the stacking lines of all the Pareto cases have been plotted together with the stacking lines resulting from using the minimum and maximum values of the chord displacement angle κ_i and blade passage distance d_i . As is evident, all stacking lines cluster together in a relatively small region. This suggests that optimal Boxprop designs decrease blade interference between the LB and TB by sweeping them in opposite directions, more specifically the LB should be swept downstream (in the negative x-direction), while the TB should be swept upstream (in the positive x-direction). In the way the Boxprop is parametrized, this means that the chord displacement angle κ_i for the Beziér control points should be positive, as was defined in Fig. 5. A chord displacement angle distribution $\kappa(r)$ can also be calculated for each position along the blade stacking line in a manner similar to how the stacking line control points are constructed. This chord displacement angle distribution has been plotted in Fig. 15 for each Pareto front design.

As can be seen, $\kappa(r)$ ranges from roughly 30 to 45 degrees at the 75% radial reference position, with an average of 41 degrees. As mentioned earlier, the design variable ranges for the chord displacement angles κ_i are strictly positive, as is seen in Table 3, so another expanded optimization was performed in order to confirm that the optimal Boxprop designs indeed fall into that range. This expanded optimization included a wider range of κ_i , and the stacking lines of its Pareto front designs are shown in Fig. 16. Here the same overall behavior can be seen as in Fig. 14, thereby confirming that the LB should be swept downstream, while the TB should be swept upstream. There are a couple of exceptions to this, as can be seen close to the hub where some designs feature blades swept in the opposite direction. This is also evident in the displacement angle distribution $\kappa(r)$ in Fig. 17, where some designs have negative values in areas of the stacking line between the hub and the $r/R = 0.5$ position. This small localized area of negative $\kappa(r)$ should not lead to any major impact on performance, as the blade interference is most pronounced in the upper half of the blade, where the relative Mach number and aerodynamic loading are high.

3.1 Fixed thrust coefficient results

A design with a thrust coefficient of $C_T = 0.486$, individual BP1112 from the Pareto front in Fig. 12, will now be analyzed in greater detail. The thrust level has been chosen to match the thrust coefficient of $C_T = 0.482$ of the legacy GPX701 Boxprop in order to highlight the decrease in losses relative to the legacy design. A wake analysis of the BP1112 design reveals that the achieved increase in propeller efficiency of 7% is mainly due to decreased levels of entropy lost work and swirl kinetic energy, as is shown in Fig. 18. As mentioned previously, the legacy Boxprop GPX701 featured blade halves that were quite close to each other and suffered from extensive blade interference effects, leading to high levels of swirl. The decreased blade interference for the new optimized BP1112 is visible in Fig. 13b, where the suction side of LB does not extend towards the TB, allowing both blade halves to operate relatively independently and resulting in less generated swirl. Also, the lower Mach numbers lead to weaker shocks, which partly explains the decrease in entropy lost work seen in Fig. 18. The sweeping of the LB and TB in opposite directions is as mentioned earlier the key geometric feature for reducing blade interference effects.

The aerodynamic optimization of the Boxprop has significantly improved its performance by decreasing the amount of generated swirl. Blade interference has been alleviated by allowing the blade to be loaded further out radially relative to the legacy Boxprop design, as is shown in Fig. 19. The new optimized Boxprop designs also feature a slightly different flowfield in the wake relative to the legacy design, as is shown in Fig. 20. Included in this figure is also the flowfield of two optimized conventional propellers with 6 and 12 blades, respectively. The choice of 6 and 12 blades for the conventional propellers allows for a more thorough comparison with the Boxprop, which for this configuration can be considered to have either 6 or 12 propeller blades depending on if the LB and TB are seen as two separate blades, or as one single blade. The optimization of the conventional propeller blades has been carried out with the same methodology as described for the Boxprop, and feature the same diameter, thickness distributions, and airfoil profiles. The optimization of the conventional propeller blades are based on baseline designs obtained with an in-house propeller design tool [25], which employs a Blade Element-Vortex method similar to the methodology

published by Drela [5]. The aerodynamic optimization aimed at maximizing the thrust coefficient and propeller efficiency, while varying chord, camber, blade angle, sweep, and lean relative to a baseline design. In Fig. 20, the vorticity magnitude has been plotted at a downstream distance of $0.2D$ from the 75% radial position of the blades which corresponds to the location of a possible downstream counter-rotating propeller. The figure shows that the radial shift in aerodynamic loading for the optimized Boxprop (BP1112) has resulted in a small vortex-like structure forming in the wake of the TB. This vortex structure is similar in extent to the tip vortex of the 12-bladed conventional propeller, but is approximately 46% weaker in terms of maximum vorticity magnitude. The development of these wake structures along the axial direction is shown for the BP1112 and the 12-bladed conventional propeller in Fig. 21, where two major observations can be made. The first observation is that the tip vortex of the conventional blade and the vortex of the Boxprop are formed differently, more specifically the Boxprop vortex is a result of the wake rolling up on itself with the vortex streamlines originating from a broad area around the blade arch tip, which then coalesce into a more compact vortex. Secondly, the tip vortex of the conventional blade is formed in a relatively small region at the blade tip, and as could be observed in Fig. 20, has higher levels of vorticity magnitude compared to the Boxprop.

The kinetic energy bounded to the wakes and tip vortices of the blades can be quantified by performing the wake analysis outlined in Eq. (14) and using the flow decomposition in Eq. (12) and (13). The individual terms inside the area integral of Eq. (14) are power fluxes, and the ones corresponding to the total kinetic energy bounded to the velocity perturbations and its components (axial, radial, tangential) are shown in Fig. 22 for planes $0.2D$ downstream of the blades. Here it is evident that the 6-bladed and 12-bladed conventional propellers feature their highest values in their tip vortices, while the optimized Boxprop has most of its perturbation kinetic energy spread out around the blade tip, with peak values occurring at its vortex. The acoustic impact of this Boxprop wake vortex during take-off conditions cannot be discerned at this stage, as it would require additional simulations to verify its existence at take-off conditions together with an appropriate acoustic analogy. At this point, it can only be noted that at cruise conditions the optimized Boxprop BP1112 features higher wake vorticity levels than the legacy GPX701, but substantially lower than what is present in the tip vortex of both the optimized 6 and 12-bladed conventional propellers, as is shown in Fig. 20.

The integrals of the loss terms of Eq. (14), namely entropy lost work, excess axial kinetic energy, average radial and swirl kinetic energy, and perturbation kinetic energy have been calculated for a plane $0.2D$ downstream of the blades, and is shown in Fig. 23. It can be seen that the optimized Boxprop lies somewhere in-between the 6-bladed and 12-bladed conventional propeller in terms of overall generation of swirl and perturbation kinetic energy. It is important to note that the swirl kinetic energy could be recoverable to some degree by a downstream counter-rotating blade, which would decrease the difference in loss magnitude between the 12-bladed conventional propeller and the Boxprop. The entropy lost work on the other hand is comparable to the 12-bladed conventional propeller, while the 6-bladed conventional propeller has slightly lower values due to weaker shocks at its tip (not shown here).

4 CONCLUSIONS

This paper has presented results from the aerodynamic optimization of the Boxprop high speed propeller. Major improvements in performance have been achieved by decreasing swirl losses and the amount of entropy lost work. The importance of minimizing these two loss sources for the Boxprop was identified using the Wake Analysis Method in a previous paper by the authors [3], and clearly showed that these two sources of loss were larger for legacy Boxprop designs than for equal-thrust conventional propeller blades. Blade interference in legacy Boxprop designs increased the amount of generated swirl due to the proximity of the blade halves to each other, and it was hypothesized that the interference could be decreased by sweeping the blades in opposite directions (see Fig. 3). This hypothesis has now been confirmed, as an increase in propeller efficiency of 7% relative to a legacy Boxprop design has been achieved by sweeping the trailing blade upstream and the leading blade downstream, decreasing blade interference and increasing the amount of thrust generated between the midspan and the tip of the blade. Analysis of the optimal designs along the obtained Pareto front show that displacement angle range for the sweeping the LB and TB of the Boxprop is between 30 and 50 degrees at midspan, which allows the LB and TB to operate without too much interference.

A vortex-like structure has been encountered on the optimized BP1112 design which was not present on the legacy Boxprop design. The extent of this vortex is similar to the extent of the tip vortex found in a comparable 12-bladed conventional propeller design, but the Boxprop vortex features significantly lower vorticity levels (46% lower). Comparing with the legacy GPX701, one can note that the new optimized Boxprop has achieved higher efficiency by increasing aerodynamic loading at higher radii, but this has come at a cost of slightly higher tip vortex strength. This suggests that the sweeping of the blade halves in opposite directions could possibly allow the designer to trade tip vortex strength for aerodynamic performance.

There is still a potential for further improving Boxprop performance in the future by employing asymmetric blades which use different thickness distributions, chord distributions, and stacking lines for each blade half. Abandoning standard airfoil profiles in favor of fully parametrized airfoils could potentially also lead to even lower losses, but would increase the number of design parameters of the design space, compounding the effect from employing asymmetric blades. The current Boxprop blades already require more design parameters (32) compared to the conventional blades (20) due to its double blade configuration, making it harder for the optimizer to find optimal Boxprop geometries than for the conventional blades. Additionally, the optimization of conventional propeller blades utilize analytically derived baseline designs which provide a good initial guess for the optimizer, which is not possible to do for the Boxprop. Nevertheless, this paper has shown that the Boxprop performance at the cruise operating point is competitive with regards to its 6 and 12-bladed conventional counterparts, especially if it would be integrated into a CROR, where swirl can be recovered in the rear counter-rotating rotor.

5 ACKNOWLEDGMENT AND FUNDING

This work was supported by Sweden's Aeronautical research program sponsored jointly by the Swedish Armed Forces, the Swedish Defense Materiel Administration and the Swedish Governmental Agency for Innovation Systems.

6 NOMENCLATURE

A	Integration area [m ²]
BEM	Blade Element Momentum method
CFD	Computational Fluid Dynamics
CROR	Counter-Rotating Open Rotor
C_T	Thrust coefficient, $C_T = F_x / \rho n^2 D^4$
D	Propeller diameter, defined from the maximum radius of the stacking line [m]
F_x	Thrust [N]
FR	Frozen Rotor interfaces
H	Flight altitude [m]
HTR	Propeller hub-to-tip-ratio
GA	Genetic Algorithm
ISA	International Standard Atmosphere
J	Advance ratio
LB	Leading Blade
LHS	Latin Hypercube Sampling
M_∞	Freestream Mach number
N_{points}	Number of sample points for the LHS
P_i	Stacking line control point i
P_{shaft}	Shaft input power [W]
R	Propeller tip radius [m]
RBF	Radial Basis Function
T	Static temperature [K]
T_∞	Static temperature far upstream [K]
TB	Trailing Blade
U_i	Circumferentially averaged velocity component i [m/s]
\dot{W}	Work done on the fluid per unit time [W]
V_∞	Velocity far upstream [m/s]
c	Airfoil chord [m]
c_{ld}	Design lift coefficient for the NACA16 airfoil profile
d_i	Passage distance parameter for stacking line control point i [m]
h	Static specific enthalpy [J/kg]

h_0	Total specific enthalpy [J/kg]
k	Turbulent kinetic energy [J/kg]
\dot{m}	Mass flow [kg/s]
n	Revolutions per second [1/s]
n_{dim}	Number of design variables χ_i
p	Static Pressure [Pa]
s	Entropy [J/(kg · K)]
r	Radius [m]
t	Blade section thickness [m]
u_i	Velocity component i [m/s]
u_n	Velocity normal to the integration surface [m/s]
v_i	Non-axisymmetric velocity perturbation component i [m/s]
y_{ave}^+	Average y^+ value for the mesh on no-slip surfaces
η	Propeller efficiency
κ	Displacement angle distribution [°]
κ_i	Displacement angle for stacking line control point P_i
ζ	Energy component [J/kg]
ρ	Density [kg/m ³]
θ	Azimuth angle [°]
ν	Specific volume [m ³ /kg]
ϕ_p	Pressure work
ϕ_s	Entropy lost work
χ_i	Design variable i

Subscripts

1	Upstream/inlet plane
2	Plane for wake evaluation
n	Normal to integration surface
r	Radial component
θ	Swirl component
x	Axial component

7 REFERENCES

- [1] Larsson, Linda, Tomas Grönstedt, and Konstantinos G. Kyprianidis. "Conceptual design and mission analysis for a geared turbofan and an open rotor configuration". In ASME 2011 Turbo Expo: Turbine Technical Conference and Exposition, Vancouver, Canada, June 6-10, 2011.
- [2] Patrao, A. Capitaó, Richard Avellán, Anders Lundbladh, and Tomas Grönstedt. "Wake and Loss Analysis for a Double Bladed Swept Propeller". In ASME Turbo Expo 2016: Turbomachinery Technical Conference and Exposition, Seoul, South Korea, June 13-17, 2016.
- [3] Patrao, A. Capitaó, Tomas Grönstedt, Richard Avellán, Anders Lundbladh, 2018, "Wake energy analysis method applied to the Boxprop propeller concept", *Aerospace Science and Technology* 79 (2018): 689-700. <https://doi.org/10.1016/j.ast.2018.06.018>.
- [4] Adkins, Charles N., and Robert H. Liebeck, 1994, "Design of optimum propellers", *Journal of Propulsion and Power* 10, no. 5, pp. 676-682.
- [5] Drela, Mark. "QPROP formulation". Massachusetts Inst. of Technology Aeronautics and Astronautics, Cambridge, MA (2006).
- [6] Negulescu, Camil A, 2013, "Airbus AI-PX7 CROR design features and aerodynamics", *SAE International Journal of Aerospace* 6, no. 2013-01-2245 (2013): 626-642.
- [7] Avellán, Richard, Alexandre Capitaó Patrao, Anders Lundbladh, and Tomas Grönstedt. "Preparing for Proof-of-concept of a Novel Propeller for Open Rotor Engines". In the 22nd International Symposium on Air Breathing Engines, Phoenix, Arizona, October 25-30, 2015, ISABE-2015-20097.
- [8] Ellbrant, Lars, Lars-Erik Eriksson, and Hans Mårtensson. "Design of compressor blades considering efficiency and stability using CFD based optimization". In ASME Turbo Expo 2012: Turbine Technical Conference and Exposition, Copenhagen, Denmark, June 11-15, 2012.
- [9] Ellbrant, Lars, Lars-Erik Eriksson, and Hans Mårtensson. "CFD optimization of a transonic compressor using multiobjective GA and metamodels". In Proceedings of the 28th International Congress of the Aeronautical Sciences, Brisbane, Australia, September 23-28, 2012.
- [10] Lejon, Marcus, Niklas Andersson, Tomas Grönstedt, Lars Ellbrant, and Hans Mårtensson. "Optimization of Robust Transonic Compressor Blades". In ASME Turbo Expo 2016: Turbomachinery Technical Conference and Exposition, Seoul, South Korea, June 13-17, 2016.
- [11] Schnell, R., J. Yin, C. Voss, and E. Nicke, 2012, "Assessment and optimization of the aerodynamic and acoustic characteristics of a counter rotating open rotor", *ASME J. Turbomach.* 134(6), p.061016.
- [12] Lepot, I., M. Leborgne, R. Schnell, J. Yin, G. Delattre, F. Falissard, and J. Talbotec, 2011, "Aero-mechanical optimization of a contra-rotating open rotor and assessment of its aerodynamic and acoustic characteristics", *Proceedings of the Institution of Mechanical Engineers, Part A: Journal of Power and Energy* 225, no. 7 (2011): 850-863.
- [14] Saravanamuttoo, Herbert Ian Howard, Gordon Frederick Crichton Rogers, and Henry Cohen. *Gas turbine theory*. Pearson Education, 2001.
- [15] Sullivan, William E., Jay E. Turnberg, and John A. Violette. *Large-Scale Advanced Prop-Fan (LAP) Blade Design*. Hamilton Standard Division, United Technologies, 1984.
- [16] ANSYS Inc, 2012, *ANSYS CFX-Solver Modelling Guide*, Version 14.5.

- [17] Deb, Kalyanmoy, Amrit Pratap, Sameer Agarwal, and T. A. M. T. Meyarivan, 2002, "A fast and elitist multiobjective genetic algorithm: NSGA-II", *IEEE transactions on evolutionary computation* 6, no. 2 (2002): 182-197.
- [18] Hall, Cesare, Alexios Zachariadis, Tobias Brandvik, and Nishad Sohoni, 2014, "How to improve open rotor aerodynamics at cruise and take-off", *The Aeronautical Journal* 118, no. 1208 (2014): 1103-1123.
- [19] Denton, J. Do. "Loss mechanisms in turbomachines." In *ASME 1993 International Gas Turbine and Aeroengine Congress and Exposition*, Cincinnati, OH, May 24-27, 1993.
- [20] Dixon, S. Larry, and Cesare Hall. *Fluid mechanics and thermodynamics of turbomachinery*. Butterworth-Heinemann, 2010.
- [21] Miller, R. J., and J. D. Denton. "Loss mechanisms in turbomachines." *Cambridge Turbomachinery Course*, University of Cambridge, Cambridge, UK (2012): 79-116.
- [22] Andersson, Jennie, Arash Eslamdoost, Alexandre Capitao Patrao, Marko Hyensjö, and Rickard E. Bensow, 2018, "Energy balance analysis of a propeller in open water", *Ocean Engineering* 158 (2018): 162-170.
- [23] Brandvik, Tobias, Cesare Hall, and Anthony B. Parry. "Angle-of-attack effects on counter-rotating propellers at take-off." In *ASME Turbo Expo 2012: Turbine Technical Conference and Exposition*, Copenhagen, Denmark, June 11-15, 2012.
- [24] Van Zante, Dale E., Fayette Collier, Arthur Orton, S. Arif Khalid, John P. Wojno, and Trevor H. Wood, 2014, "Progress in open rotor propulsors: The FAA/GE/NASA open rotor test campaign", *The Aeronautical Journal* 118, no. 1208 (2014): 1181-1213.
- [25] Capitao Patrao, Alexandre. *Implementation of Blade Element Momentum/Vortex Methods for the Design of Aero Engine Propellers*: Chalmers University of Technology, Gothenburg, 2017.

Figure Captions List

Fig. 1 – A conceptual rendering of an open rotor featuring two propeller blade rows. Air flows from left to right, the front rotor is composed of a Boxprop while the rear rotor is a conventional propeller blade. (TURBO-18-1208).

Fig. 2 - Boxprop with direction of airflow and rotation. Leading (LB) and trailing blades (TB) relative to the direction of rotation are marked.

Fig. 3 - Potential blade interference counter-measures for the Boxprop. Arrows denote the direction that blade halves can be moved. 1) Involves sweeping apart the blade halves along the flow direction, the TB upstream and LB downstream. 2) Moving the blade halves apart in the tangential direction.

Fig. 4 –The components of the Boxprop optimization platform.

Fig. 5 – The stacking line is built up for each blade half separately as is shown in the figure to the left, and they share a common control point (P_4) at the tip of the blade, which is constrained to lie on the z-axis. The position of the individual remaining control points is constructed using a displacement angle κ_i and a blade passage distance parameter d_i , as shown in the figure to the right. The arrow head of the local undisturbed velocity vector V_∞ also coincides with z- axis, and is perpendicular to the distance blade passage distance d_i .

Fig. 6 – Radial distribution of camber. The control points P_1 to P_5 are used to construct the Bézier curve which defines the camber distribution.

Fig. 7 – Domain setup for the CFD simulations. Frozen Rotor (FR) interfaces connect the inner 3D (white) and outer 2D domain (gray).

Fig. 8 –The GA structure.

Fig. 9 –Control volume for wake analysis. Surface 1 (gray) is assumed to have uniform properties while the streamsurface S (green) has no mass flux crossing it. A streamline travelling from 1 to 2 (purple) has been added to illustrate the work transfer from a propeller blade to the flow.

Fig. 10 –Simulation domain of the cases analyzed with the wake analysis theory. The red line denotes the integration surface used in the wake analysis. Identical boundary conditions are used as for the optimization cases. The downstream Frozen Rotor interface present in the optimization cases has been removed in this domain setup. Instead, the inner 3D domain has been extended axially downstream all the way to the Outlet. Note that the axial extent of the outer 2D domain is not exactly the same as for the optimization cases. The optimization cases used a domain size identical to a previous optimization paper [13], while the wake analysis cases use an outer domain size in line with what was used in a previous Boxprop wake analysis paper [3].

Fig. 11 –Coarsest (9.9M cells) mesh used for the Boxprop wake energy analysis mesh study. The freestream flow direction is aligned with the negative x-axis. As can be seen, the blocks downstream of the blade trailing edge are well refined in order to capture the sharp gradients of the wakes.

Fig. 12 –Results for the aerodynamic optimization of a 6-blade Boxprop, Pareto front shown in green. A scaled up legacy Boxprop (GPX701) propeller simulation from a previous study has been included in order to illustrate the propeller efficiency improvement. A design (BP1112) from the Pareto front with a C_T value close to the GPX701 has been re-simulated with a fine mesh (1112_FM) and shows an improvement of 7% in propeller efficiency.

Fig. 13 –Mach number distributions at 75% radius for the legacy GPX701 Boxprop (top) and the optimized BP1112 design (bottom).

Fig. 14 – LB (solid green) and TB (solid black) stacking lines for all the cases in the Pareto front of the optimization. The dashed lines are the limits in stacking line positions for the LB (green) and TB (black) resulting from using the min/max values of the chord displacement angle κ_i and blade passage distance d_i .

Fig. 15 – Calculated displacement angle $\kappa(r)$ distribution for each position of the stacking line. Curves in grey denote the displacement angle distributions of each individual Pareto front design while the green line denotes the average of the entire Pareto front.

Fig. 16 - LB (solid green) and TB (solid black) stacking lines for all the cases in the Pareto front of an optimization with broader variable ranges for the stacking line displacement angle κ_i and blade passage distance d_i . The dashed lines are the limits in stacking line positions for the LB (green) and TB (black) resulting from using the min/max values of κ_i and d_i .

Fig. 17 - Calculated displacement angle $\kappa(r)$ distribution for each position of the stacking line for all the cases in the Pareto front of an optimization with broader variable ranges. Curves in grey denote the displacement angle distributions of each individual Pareto front design in the expanded optimization, while the green line denotes the average of the entire Pareto front.

Fig. 18 - The levels of entropy lost work ϕ_s , radial kinetic energy $u_r^2/2$, swirl kinetic energy $u_\theta^2/2$, and excess axial kinetic energy $(\Delta u_x)^2/2$ for the GPX701 and BP1112. These correspond to the loss terms in Eq. (11), and are integrated on a surface located at a downstream axial distance of $0.05D$ from the trailing edge at the 75% radius position.

Fig. 19 – Sectional lift distribution along the radius of the blades for the legacy GPX701 Boxprop, optimized BP1112 Boxprop, the 6-bladed conventional propeller, and the 12-bladed conventional propeller.

Fig. 20 – Vorticity [$1/s$] contour plots for the a) legacy GPX701 Boxprop, b) optimized BP1112 Boxprop, c) optimized 6-bladed conventional propeller, and d) optimized 12-bladed conventional propeller.

Fig. 21 – Axial cuts of wake vorticity (blue) and vortex streamlines (red) for the BP1112 (upper image) and the optimized 12-bladed conventional propeller (lower image). The axial cuts range downstream axial distances of $0.05D$ to $0.525D$ from the trailing edge of the blades (at $r/R=0.75$).

Fig. 22 – Power fluxes (W/m^2) in descending vertical order for the legacy GPX701 Boxprop, BP1112 optimized Boxprop, 6-bladed conventional propeller, and the 12-bladed conventional propeller. The power fluxes represent the fluxes of kinetic energy due to the velocity perturbations, and are plotted on planes located $0.2D$ downstream of the propellers. The displayed values have been scaled with a factor 10^5 .

Fig. 23 – The magnitudes of the various loss sources for the propellers. The losses are presented as percentages of the engine shaft power for each propeller.

Table Caption List

Table 1 – Integration surface size effect on the wake analysis terms. The values are written as percentages of shaft power, and calculated as the finite difference relative to the largest surface (Surf 4). The surfaces of integration are located $0.05D$ from the trailing edge of the BP1112 Boxprop at $r/R=0.75$.

Table 2 - Operating point and propeller properties for the aerodynamic optimization.

Table 3 – Chord displacement angle κ_i ranges for the optimization presented in this paper and an additional, expanded optimization where the ranges of κ_i have been increased.

8 FIGURES

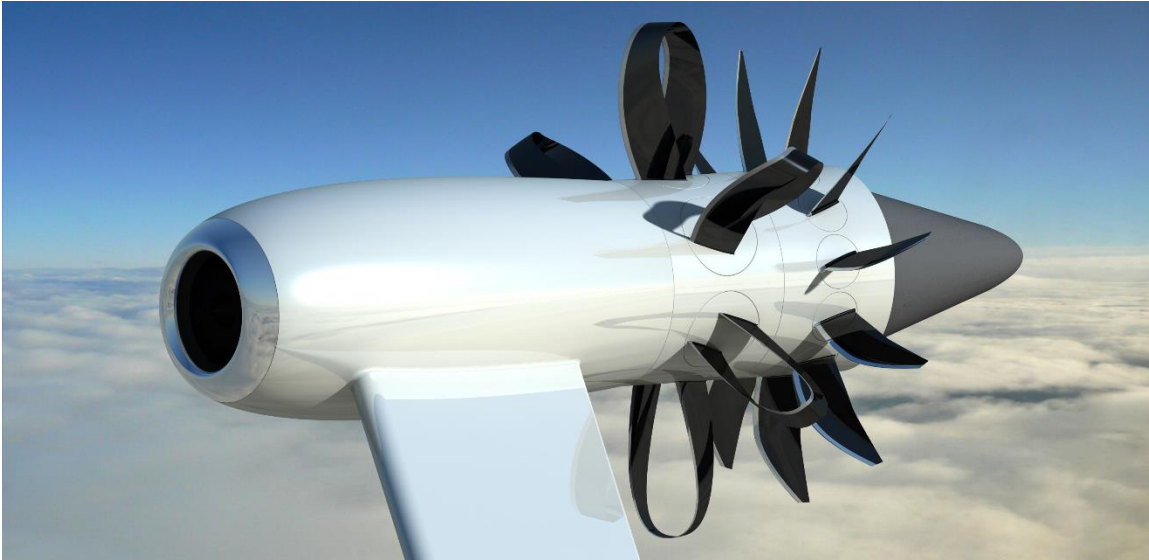


Fig. 1 – A conceptual rendering of an open rotor featuring two propeller blade rows. Air flows from left to right, the front rotor is composed of a Boxprop while the rear rotor is a conventional propeller blade.

1 COLUMN WIDTH

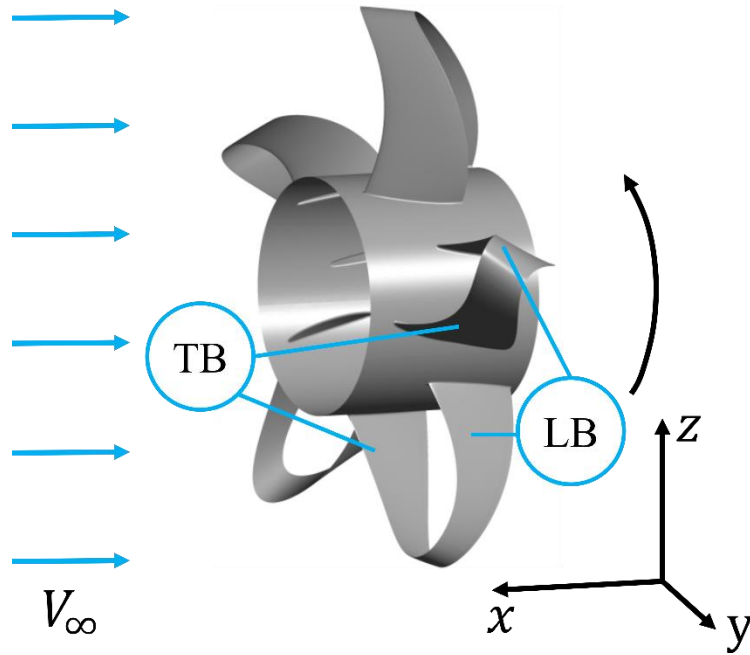
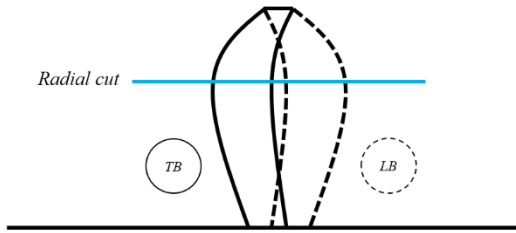


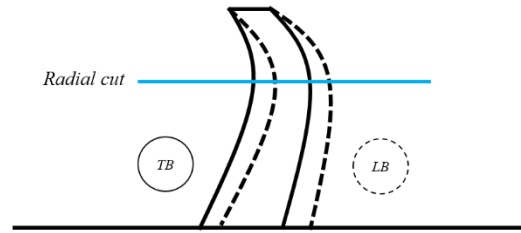
Fig. 2 - Boxprop with direction of airflow and rotation. Leading (LB) and trailing blades (TB) relative to the direction of rotation are marked.

1 COLUMN WIDTH

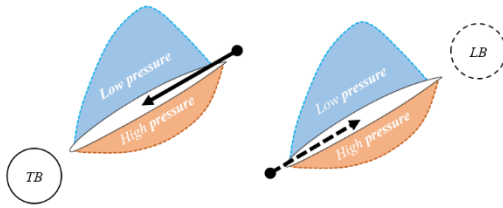
1) Planform



2) Planform



1) Radial cut



2) Radial cut

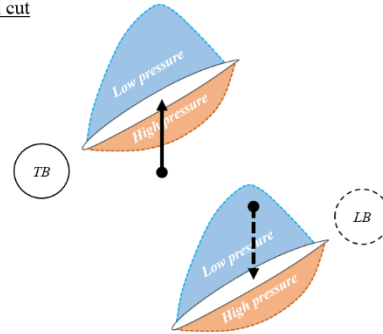


Fig. 3 - Potential blade interference counter-measures for the Boxprop. Arrows denote the direction that blade halves can be moved. 1) Involves sweeping apart the blade halves along the flow direction, the TB upstream and LB downstream. 2) Moving the blade halves apart in the tangential direction.

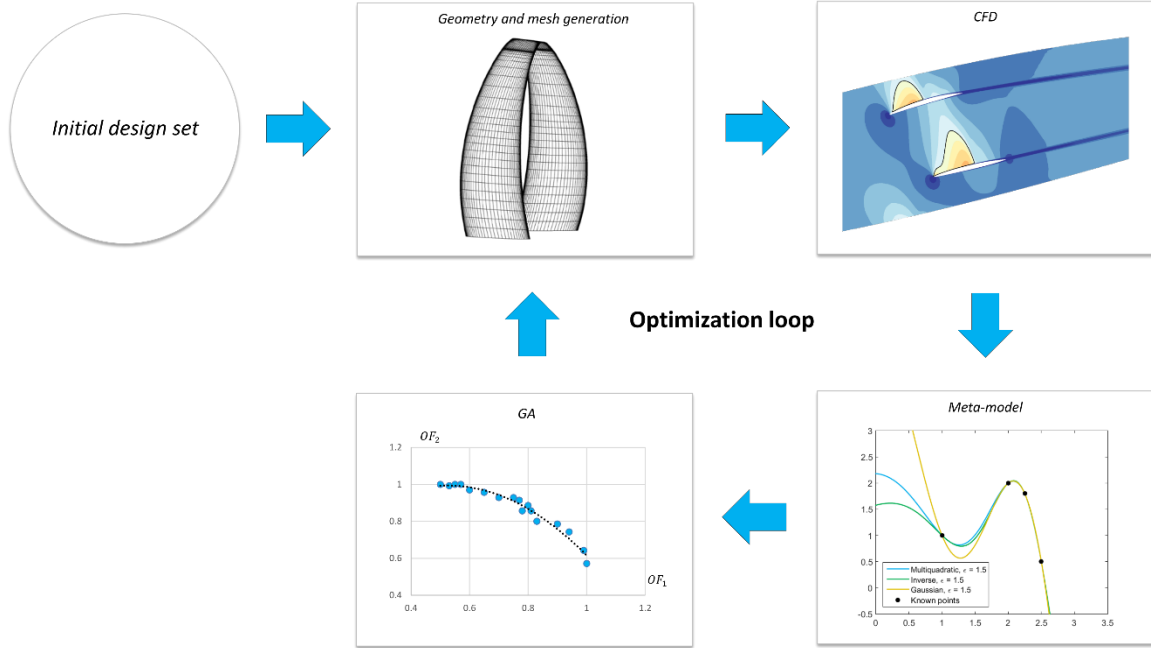


Fig. 4 –The components of the Boxprop optimization platform.

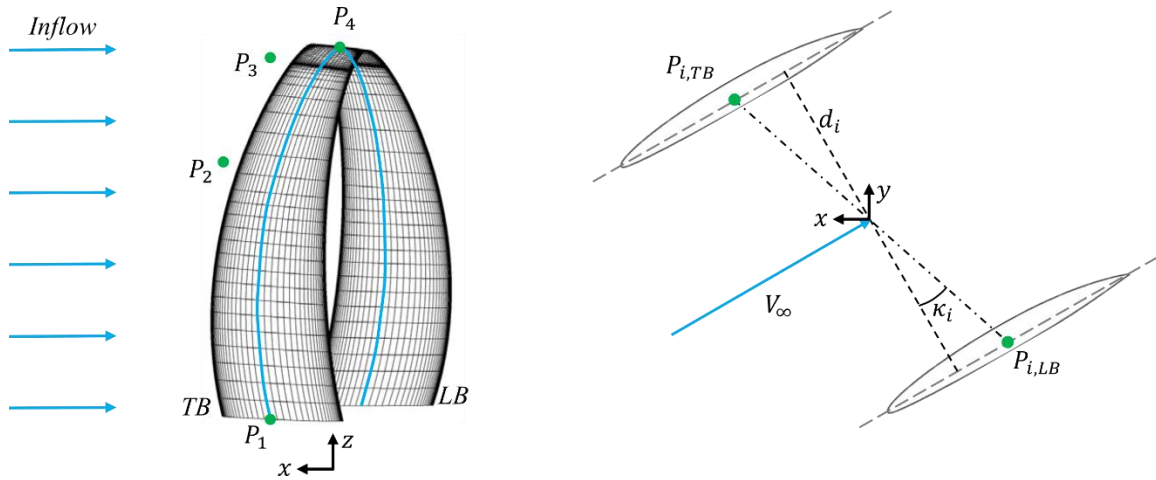


Fig. 5 – The stacking line is built up for each blade half separately as is shown in the figure to the left, and they share a common control point (P_4) at the tip of the blade, which is constrained to lie on the z -axis. The position of the individual remaining control points is constructed using a displacement angle κ_i and a blade passage distance parameter d_i , as shown in the figure to the right. The arrow head of the local undisturbed velocity vector V_∞ also coincides with z -axis, and is perpendicular to the distance blade passage distance d_i .

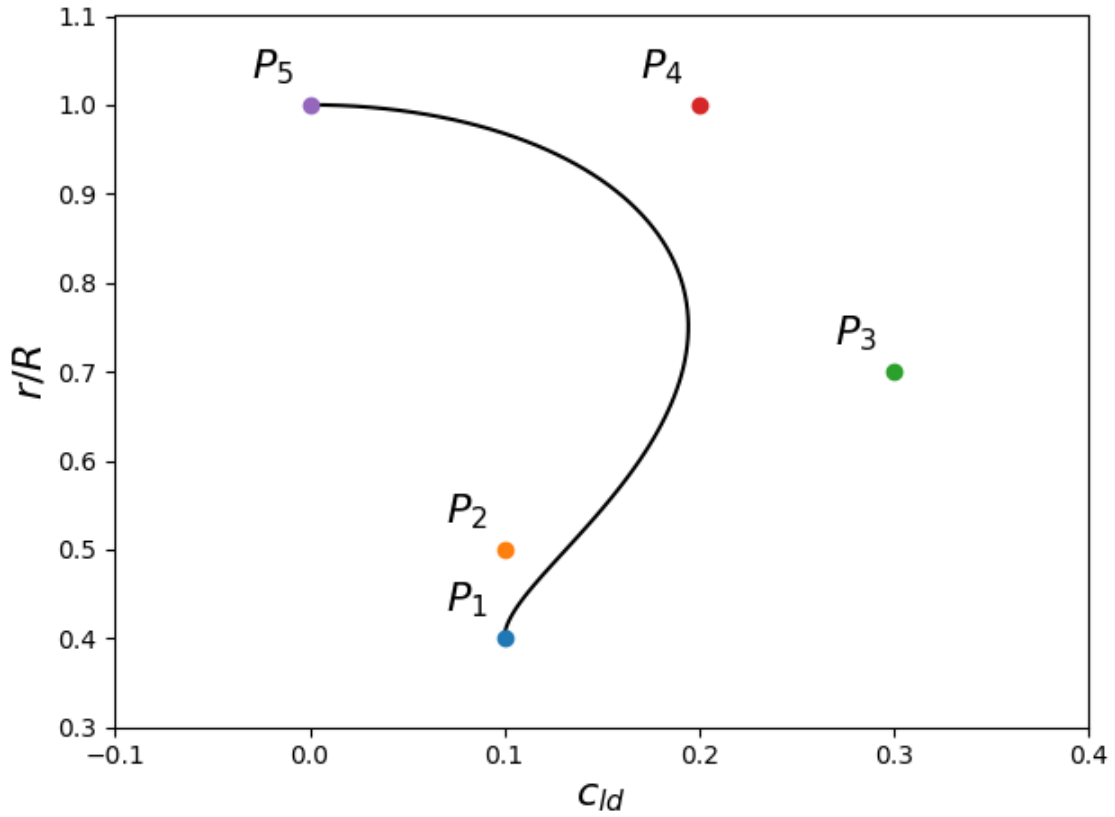


Fig. 6 – Radial distribution of camber. The control points P_1 to P_5 are used to construct the Bézier curve which defines the camber distribution.

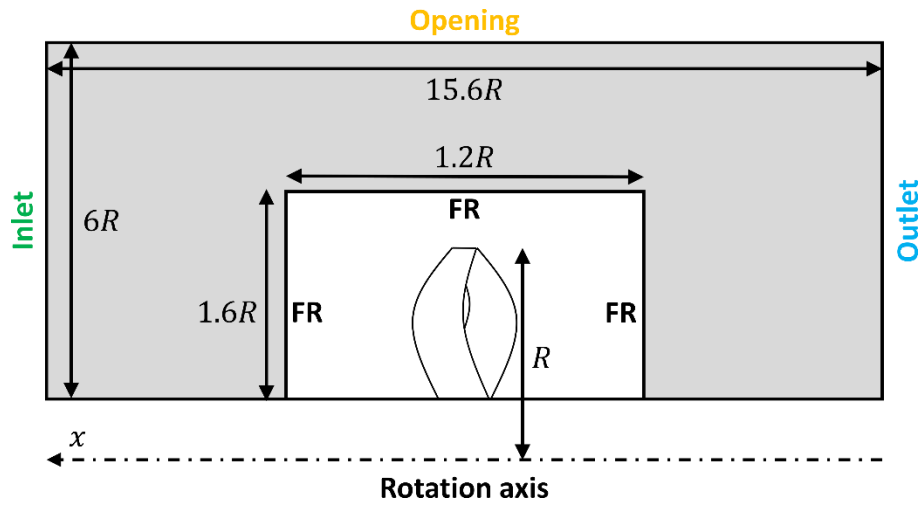


Fig. 7 – Domain setup for the CFD simulations. Frozen Rotor (FR) interfaces connect the inner 3D (white) and outer 2D domain (gray).

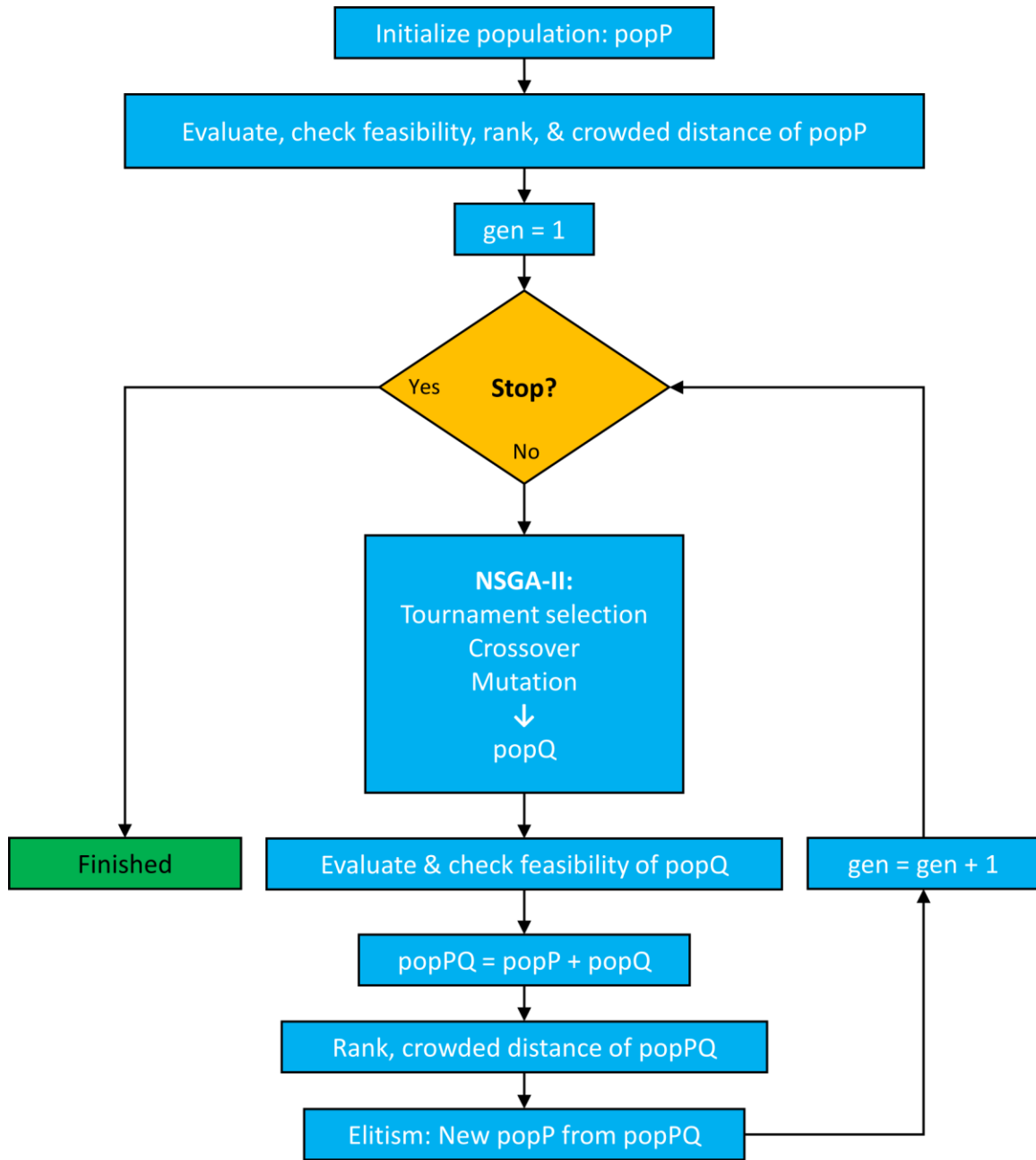


Fig. 8 –The GA structure.

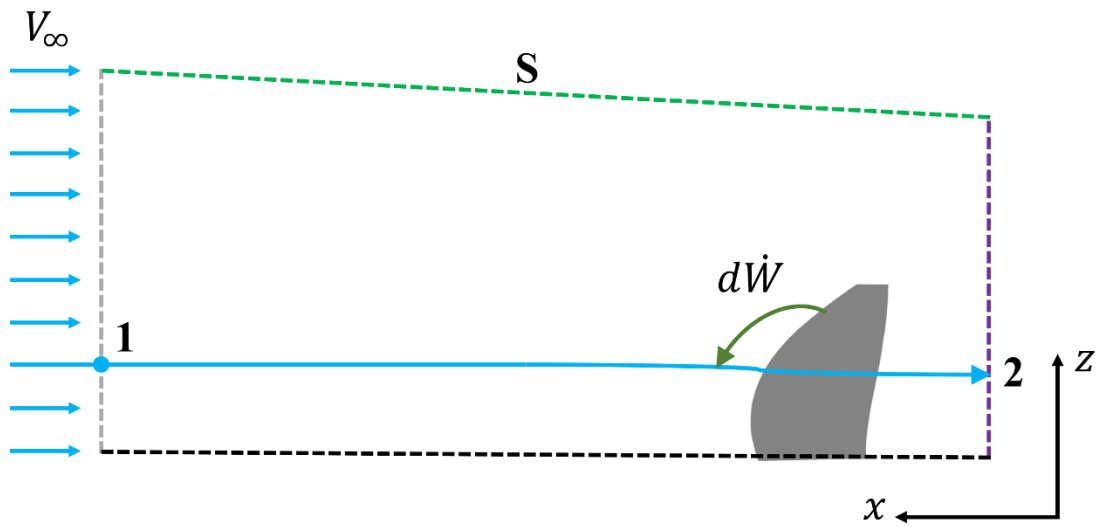


Fig. 9—Control volume for wake analysis. Surface 1 (gray) is assumed to have uniform properties while the streamsurface S (green) has no mass flux crossing it. A streamline travelling from 1 to 2 (purple) has been added to illustrate the work transfer from a propeller blade to the flow.

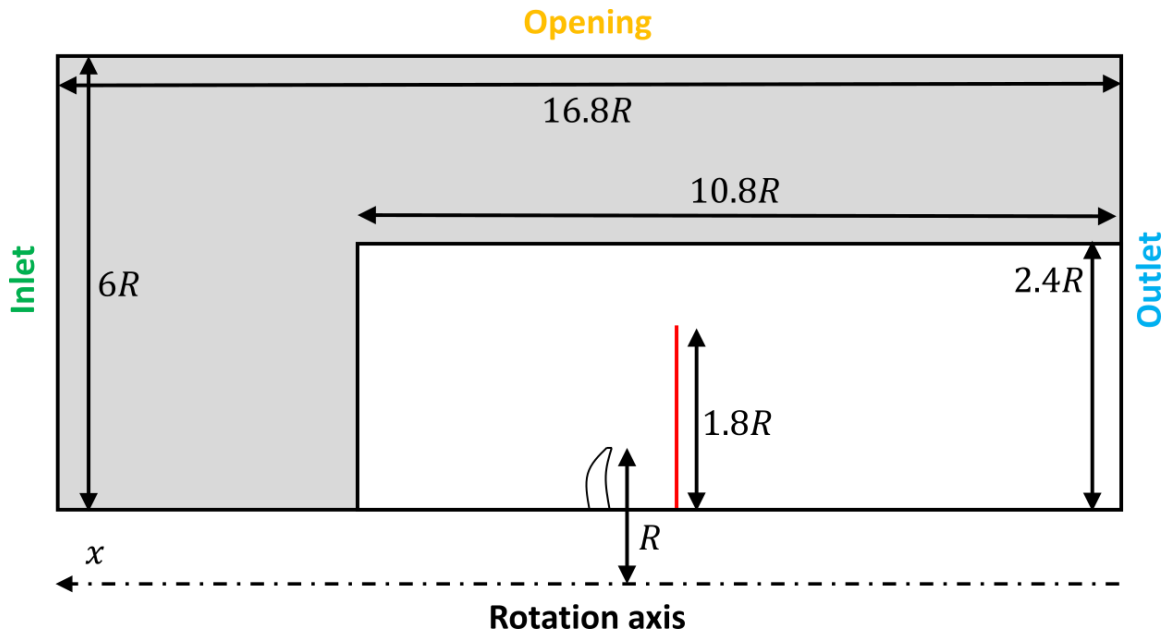


Fig. 10 –Simulation domain of the cases analyzed with the wake analysis theory. The red line denotes the integration surface used in the wake analysis. Identical boundary conditions are used as for the optimization cases. The downstream Frozen Rotor interface present in the optimization cases has been removed in this domain setup. Instead, the inner 3D domain has been extended axially downstream all the way to the Outlet. Note that the axial extent of the outer 2D domain is not exactly the same as for the optimization cases. The optimization cases used a domain size identical to a previous optimization paper [13], while the wake analysis cases use an outer domain size in line with what was used in a previous Boxprop wake analysis paper [3].

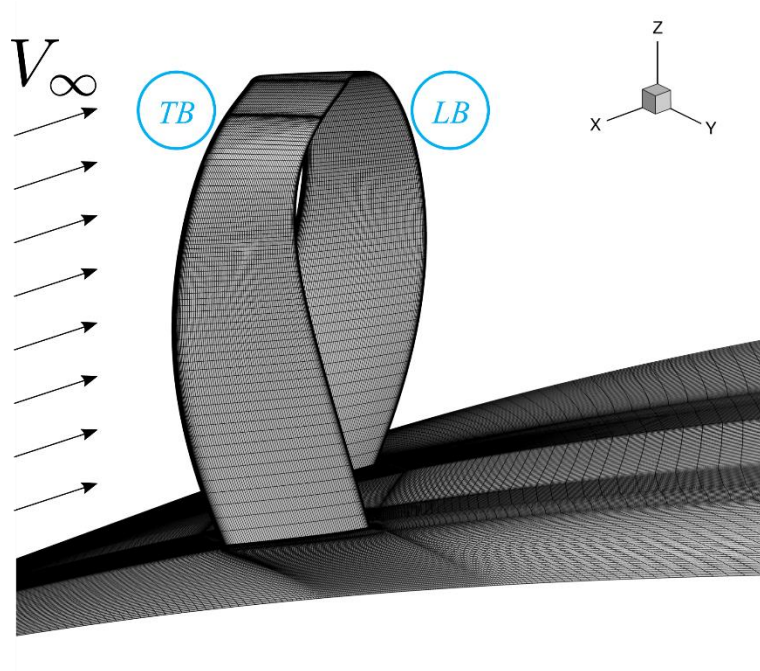


Fig. 11 –Coarsest (9.9M cells) mesh used for the Boxprop wake energy analysis mesh study. The freestream flow direction is aligned with the negative x-axis. As can be seen, the blocks downstream of the blade trailing edge are well refined in order to capture the sharp gradients of the wakes.

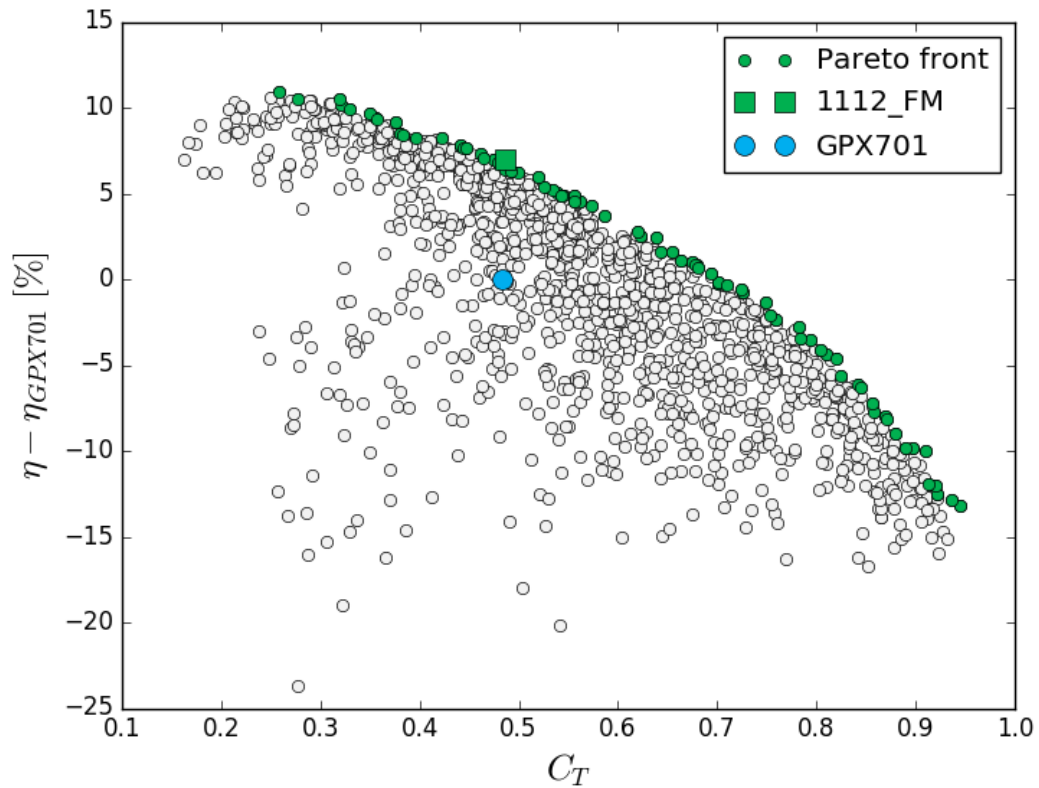


Fig. 12 –Results for the aerodynamic optimization of a 6-blade Boxprop, Pareto front shown in green. A scaled up legacy Boxprop (GPX701) propeller simulation from a previous study has been included in order to illustrate the propeller efficiency improvement. A design (BP1112) from the Pareto front with a C_T value close to the GPX701 has been re-simulated with a fine mesh (1112_FM) and shows an improvement of 7% in propeller efficiency.

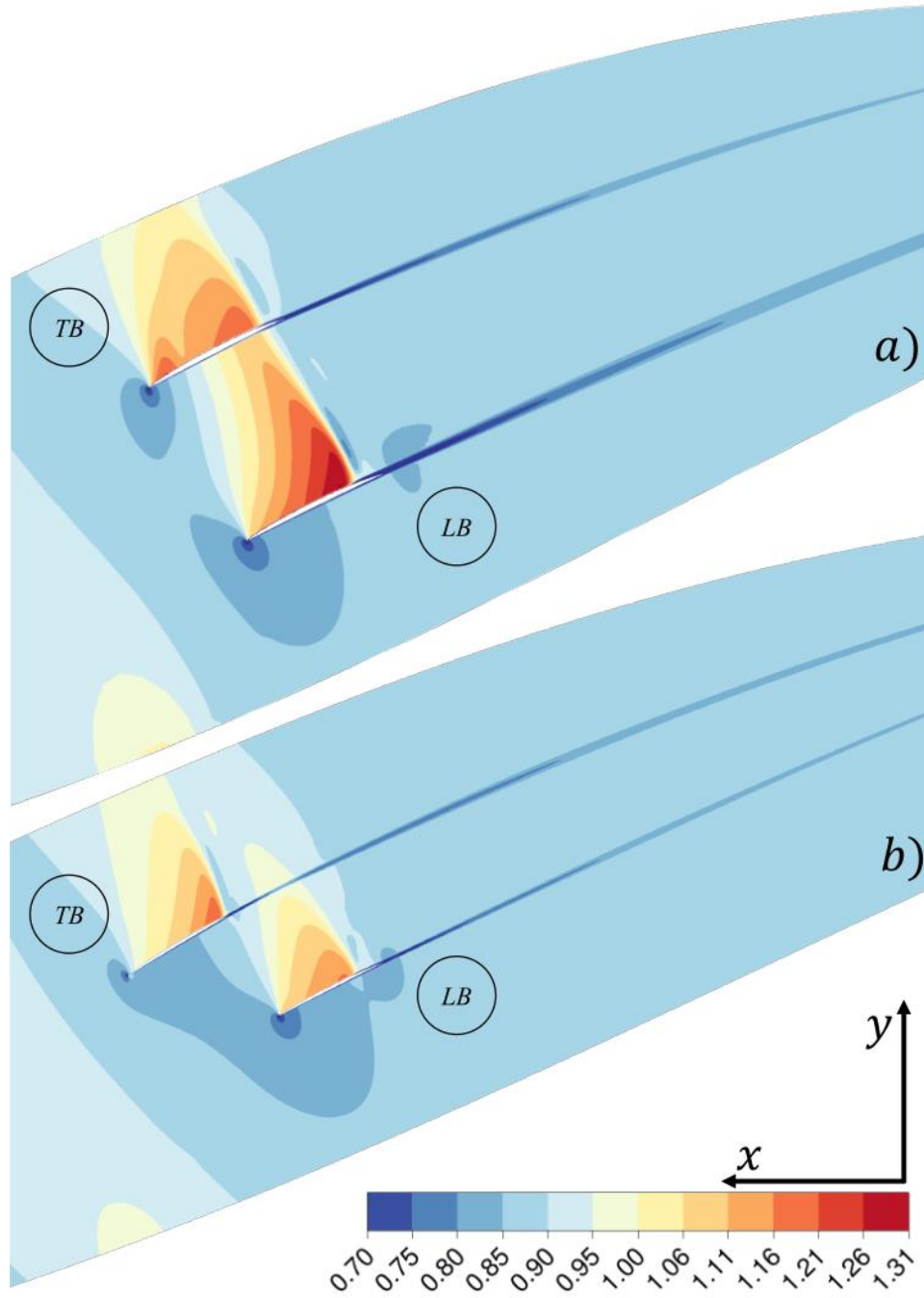


Fig. 13 –Mach number distributions at 75% radius for the legacy GPX701 Boxprop (top) and the optimized BP1112 design (bottom).

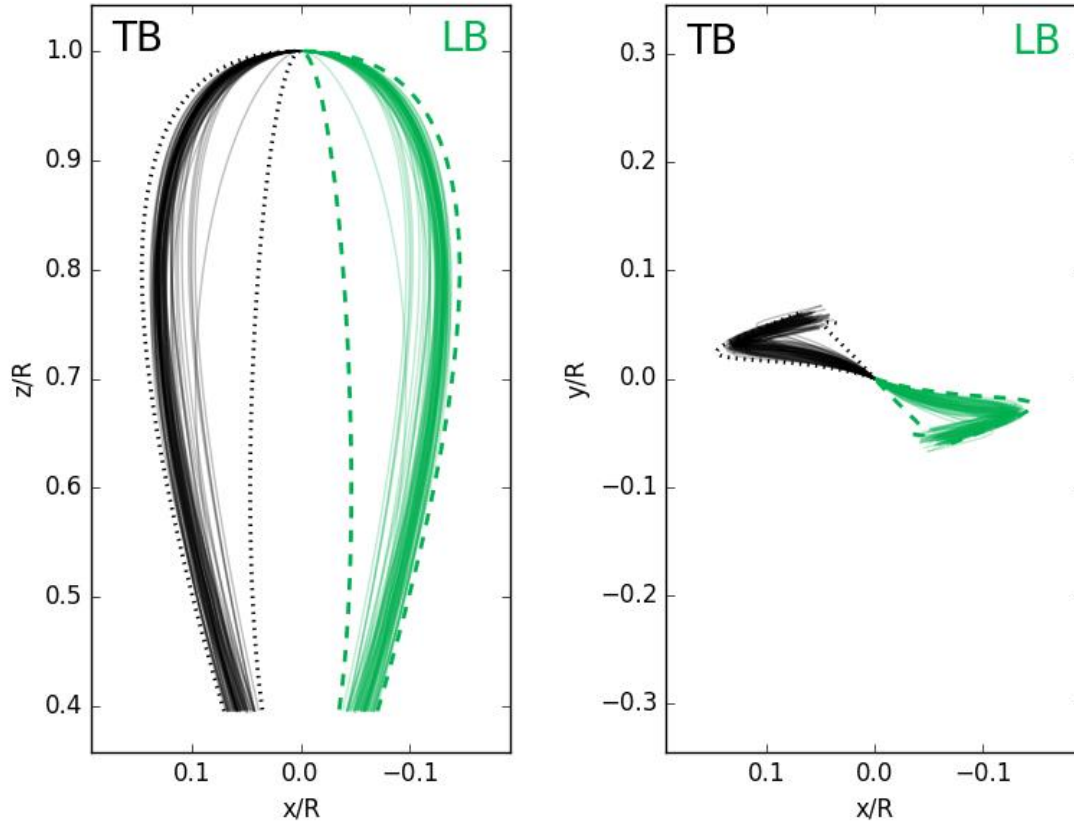


Fig. 14 – LB (solid green) and TB (solid black) stacking lines for all the cases in the Pareto front of the optimization. The dashed lines are the limits in stacking line positions for the LB (green) and TB (black) resulting from using the min/max values of the chord displacement angle κ_i and blade passage distance d_i . Note the flipped x -axis, in order to be consistent with previous Boxprop images where the undisturbed flow goes from left to right.

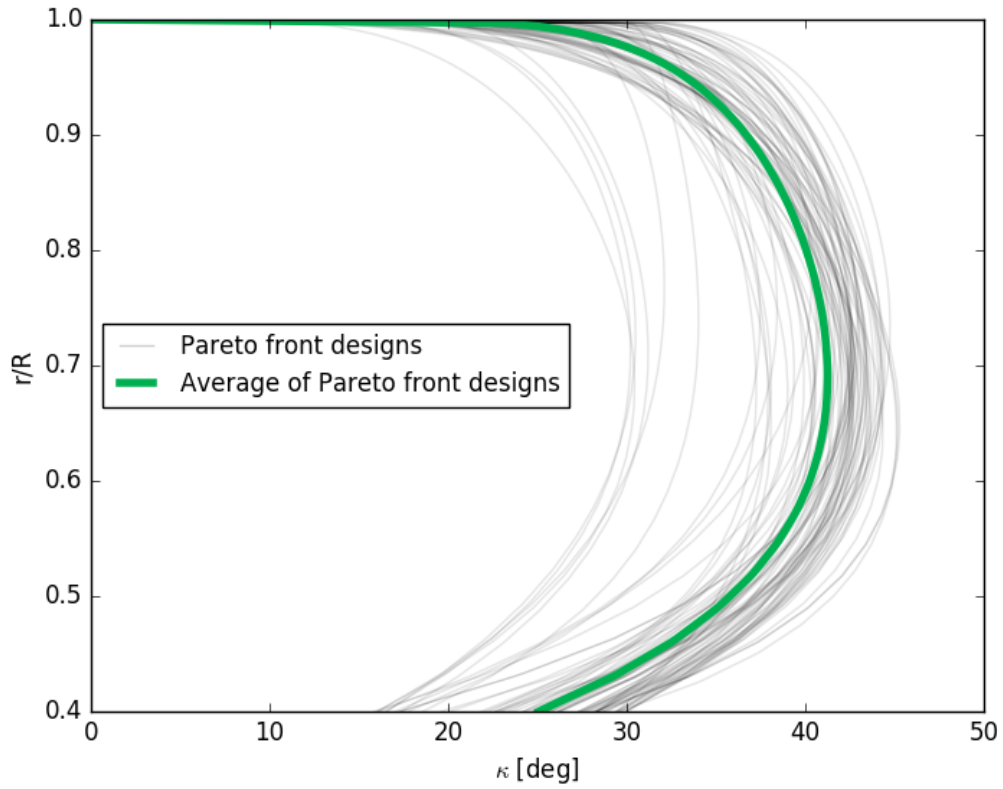


Fig. 15 – Calculated displacement angle $\kappa(r)$ distribution for each position of the stacking line. Curves in grey denote the displacement angle distributions of each individual Pareto front design while the green line denotes the average of the entire Pareto front.

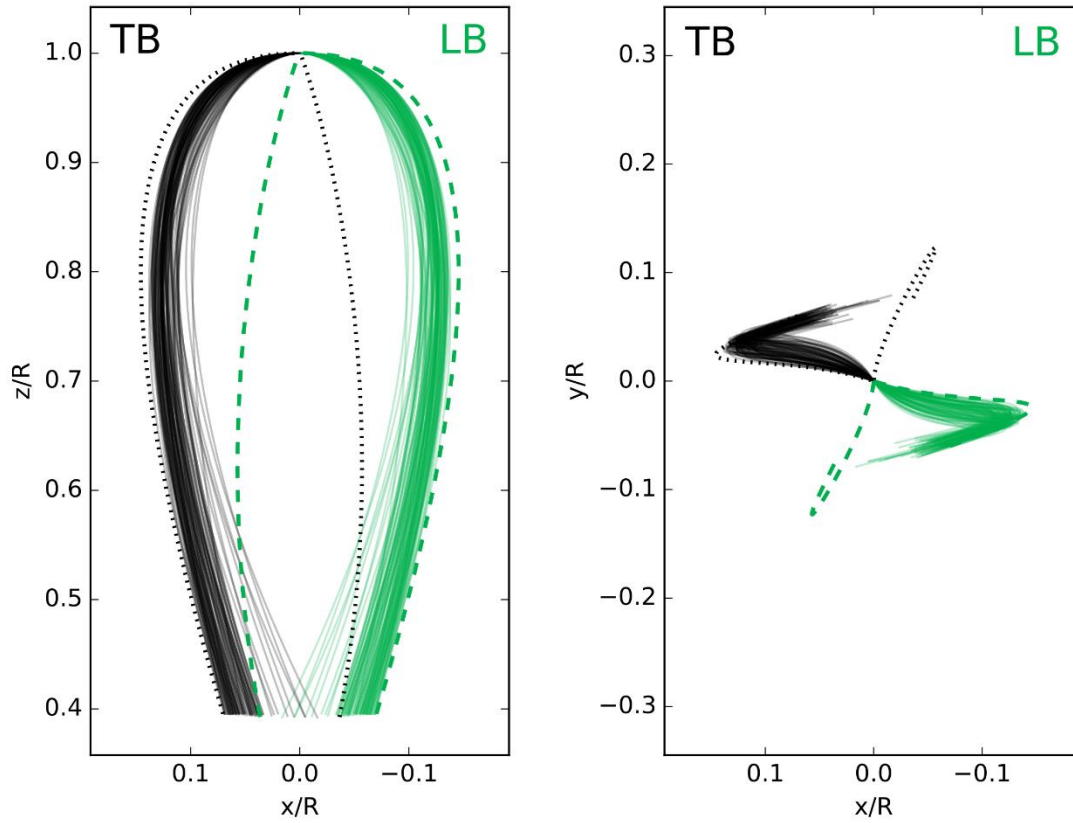


Fig. 16 - LB (solid green) and TB (solid black) stacking lines for all the cases in the Pareto front of an optimization with broader variable ranges for the stacking line displacement angle κ_i and blade passage distance d_i . The dashed lines are the limits in stacking line positions for the LB (green) and TB (black) resulting from using the min/max values of κ_i and d_i . Note the flipped x-axis, in order to be consistent with previous Boxprop images where the undisturbed flow goes from left to right.

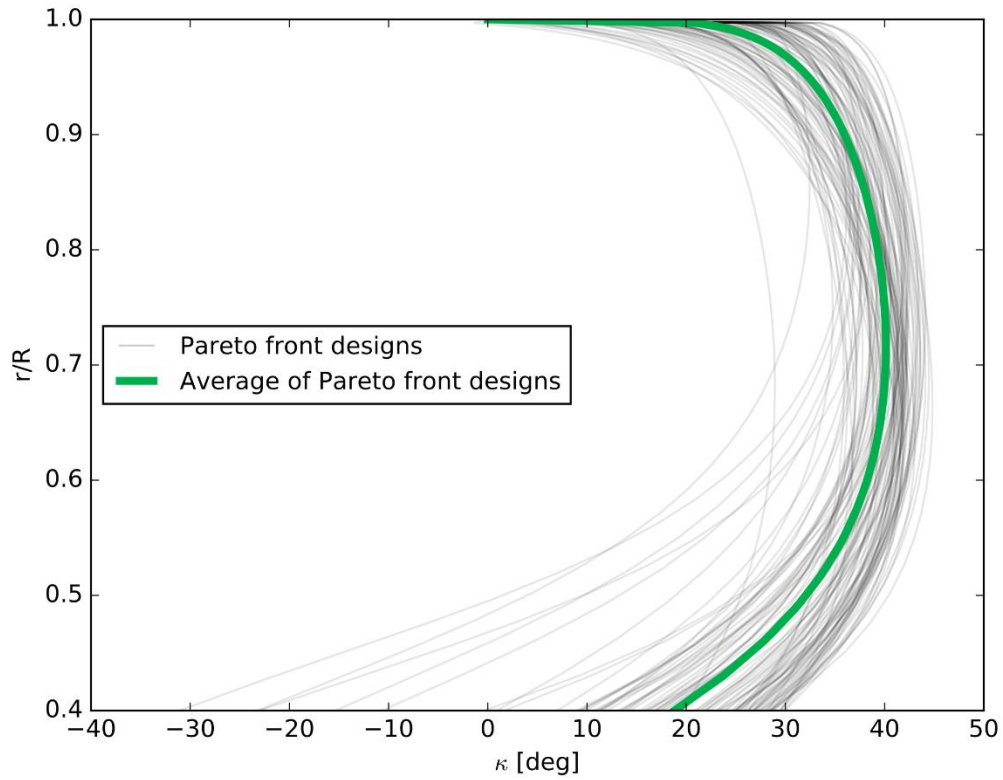


Fig. 17 - Calculated displacement angle $\kappa(r)$ distribution for each position of the stacking line for all the cases in the Pareto front of an optimization with broader variable ranges. Curves in grey denote the displacement angle distributions of each individual Pareto front design in the expanded optimization, while the green line denotes the average of the entire Pareto front.

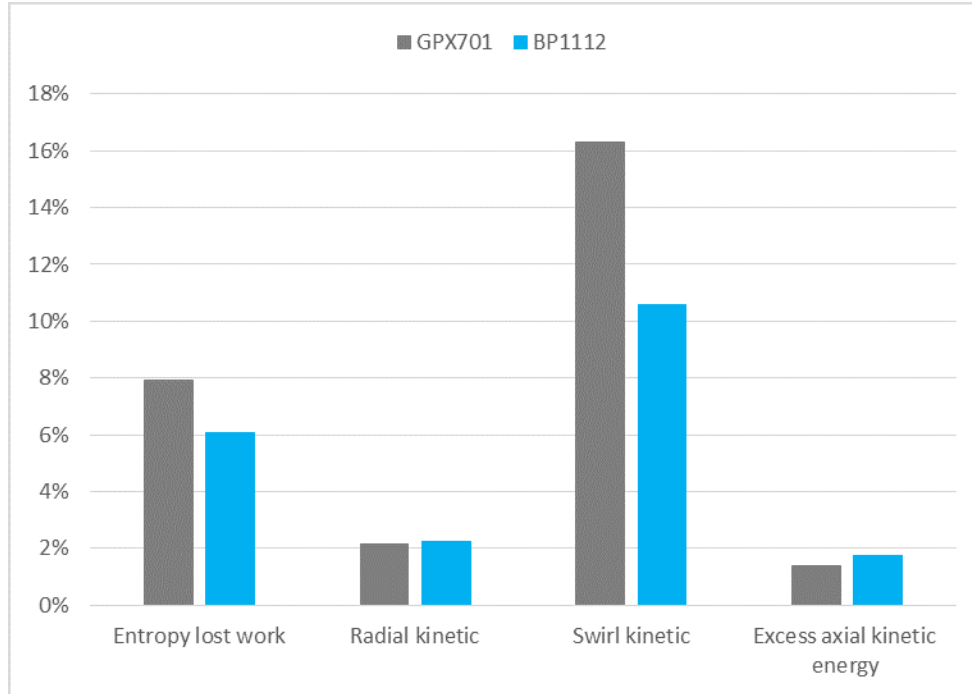


Fig. 18 - The levels of entropy lost work ϕ_s , radial kinetic energy $u_r^2/2$, swirl kinetic energy $u_\theta^2/2$, and excess axial kinetic energy $(\Delta u_x)^2/2$ for the GPX701 and BP1112. These correspond to the loss terms in Eq. (11), and are integrated on a surface located at a downstream axial distance of $0.05D$ from the trailing edge at the 75% radius position. The values have been normalized with shaft power P_{shaft} .

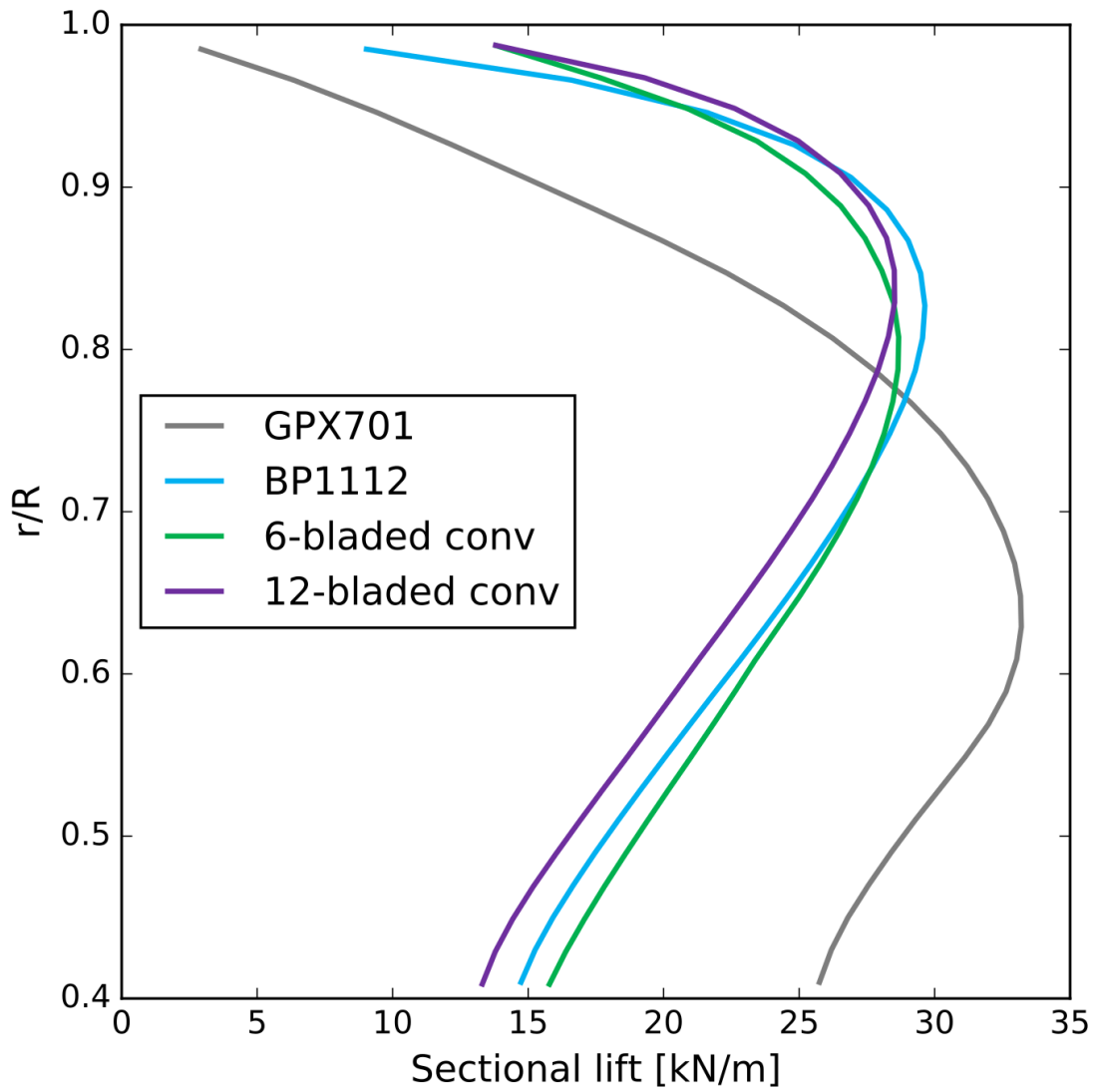


Fig. 19 – Sectional lift distribution along the radius of the blades for the legacy GPX701 Boxprop, optimized BP1112 Boxprop, the 6-bladed conventional propeller, and the 12-bladed conventional propeller.

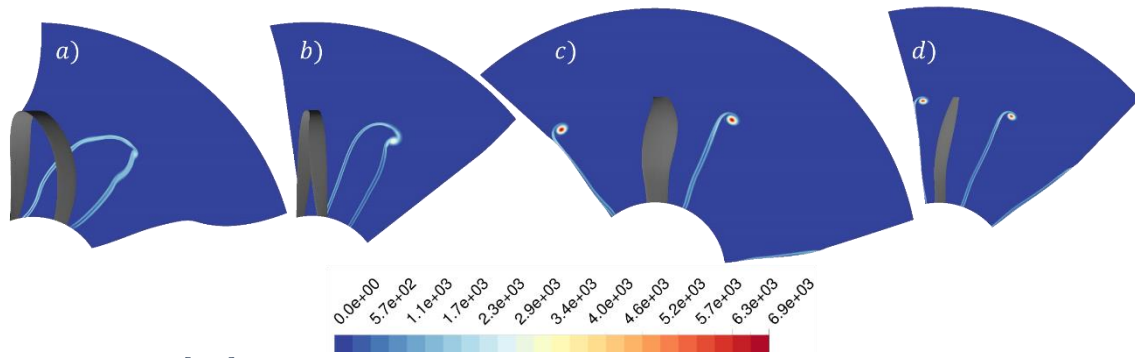


Fig. 20 – Vorticity [1/s] contour plots for the a) legacy GPX701 Boxprop, b) optimized BP1112 Boxprop, c) optimized 6-bladed conventional propeller, and d) optimized 12-bladed conventional propeller. The planes are located at $0.2D$ downstream of the trailing edge of the blades (at $r/R=0.75$).

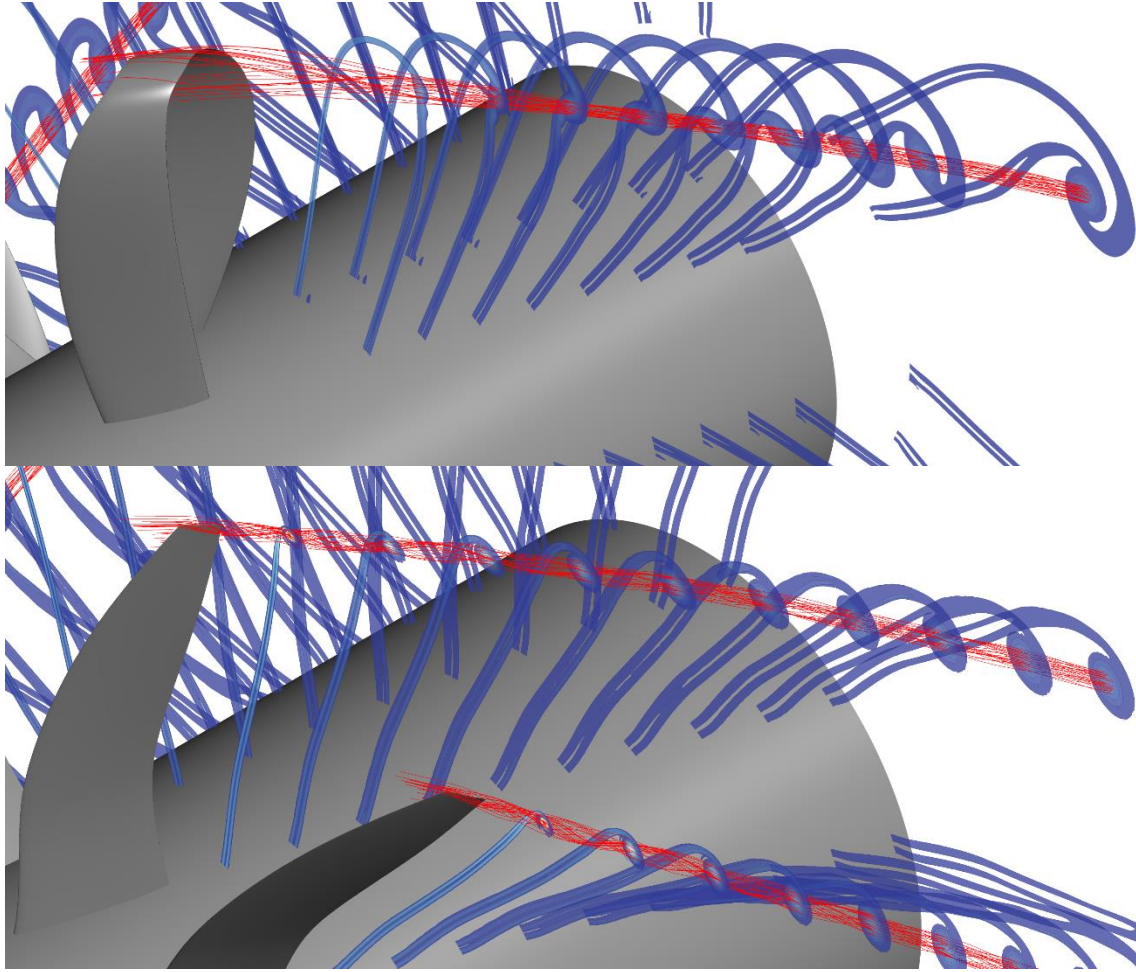


Fig. 21 – Axial cuts of wake vorticity (blue) and vortex streamlines (red) for the BP1112 (upper image) and the optimized 12-bladed conventional propeller (lower image). The axial cuts range downstream axial distances of $0.05D$ to $0.525D$ from the trailing edge of the blades (at $r/R=0.75$).

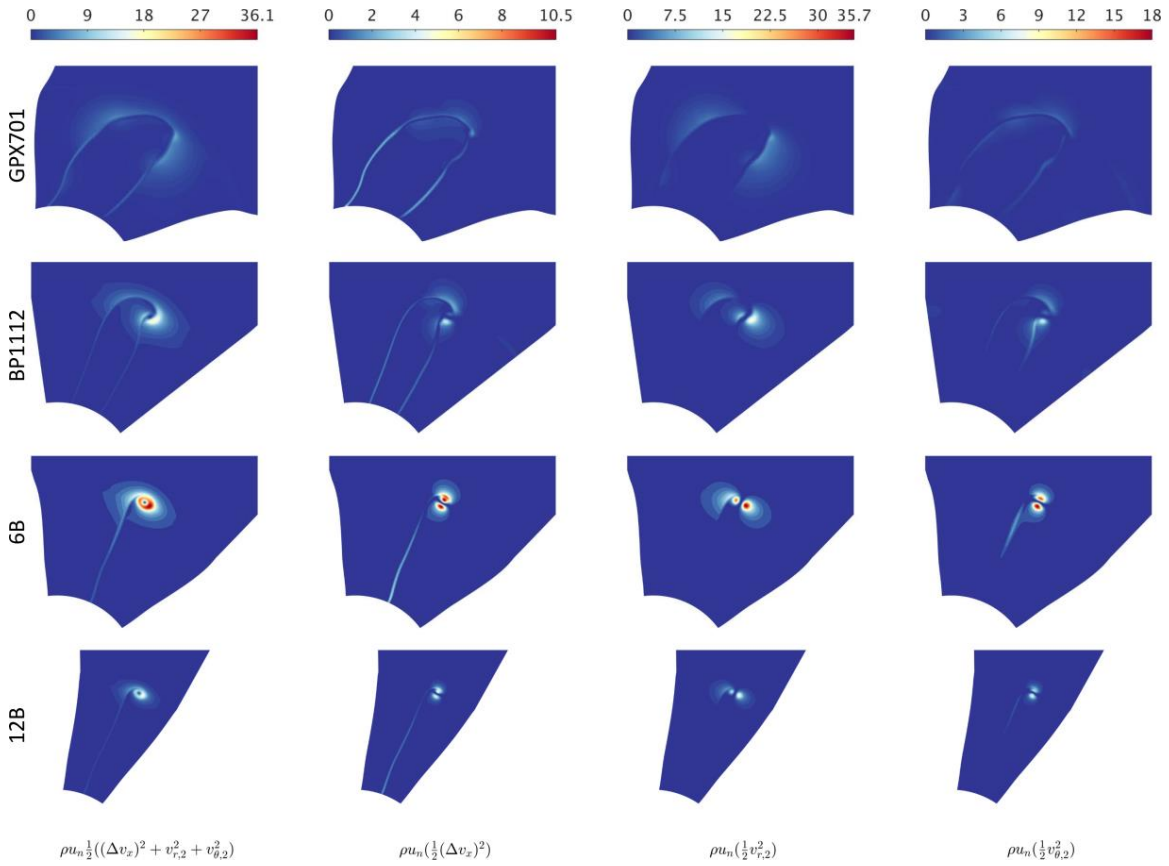


Fig. 22 – Power fluxes (W/m^2) in descending vertical order for the legacy GPX701 Boxprop, BP1112 optimized Boxprop, 6-bladed conventional propeller, and the 12-bladed conventional propeller. The power fluxes represent the fluxes of kinetic energy due to the velocity perturbations, and are plotted on planes located $0.2D$ downstream of the propellers. The displayed values have been scaled with a factor 10^5 .

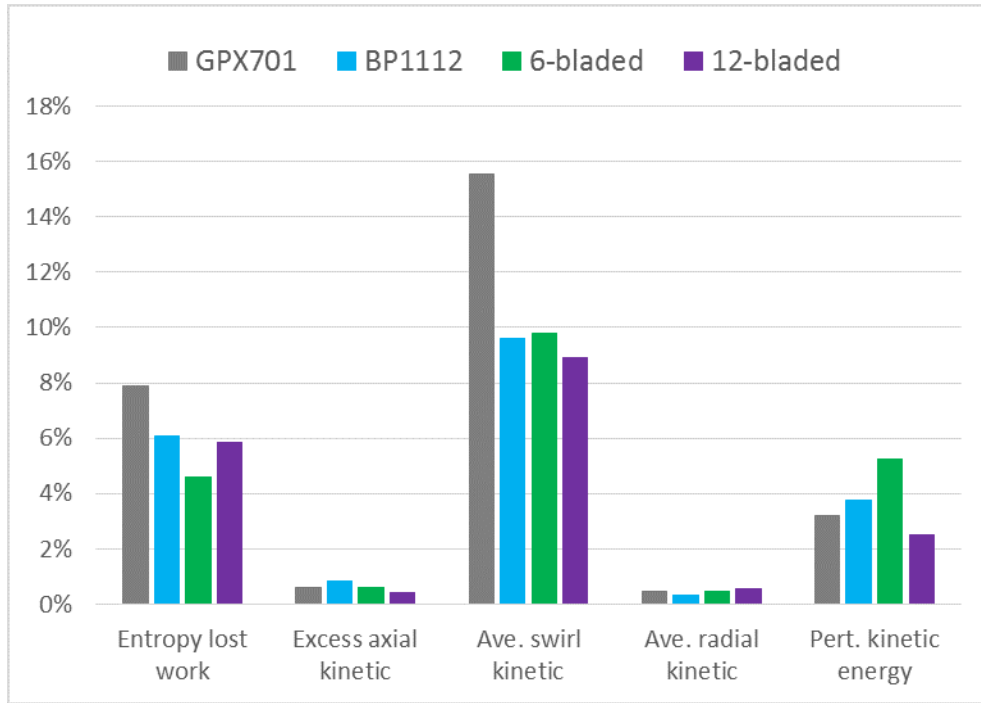


Fig. 23 – The magnitudes of the various loss sources for the propellers. The losses are presented as percentages of the engine shaft power for each propeller.

9 TABLES

Table 1 – Integration surface size effect on the wake analysis terms. The values are written as percentages of shaft power, and calculated as the finite difference relative to the largest surface (Surf 4). The surfaces of integration are located 0.05D from the trailing edge of the BP1112 Boxprop at $r/R=0.75$.

$\frac{1}{P_{shaft}} \int_2 \zeta d\dot{m}$	Difference in integral values vs Plane 4			
	Surf 1 1.2R	Surf 2 1.5R	Surf 3 1.8R	Surf 4 2.1R
Δh_0	-0.09%	-0.03%	-0.03%	-
ϕ_s	-0.10%	-0.10%	-0.07%	-
ϕ_p	-8.70%	-4.18%	-1.54%	-
$\zeta = u_{x,1} \Delta u_x$	+9.19%	+4.56%	+1.71%	-
$\phi_p + u_{x,1} \Delta u_x$	+0.49%	+0.38%	+0.18%	-
$(\Delta u_x)^2 / 2$	-0.16%	-0.11%	-0.04%	-
$u_r^2 / 2$	-0.25%	-0.16%	-0.08%	-
$u_\theta^2 / 2$	-0.07%	-0.04%	-0.01%	-

Table 2 - Operating point and propeller properties for the aerodynamic optimization.

<i>Number of blades:</i>	6
<i>J</i>	3.56
<i>M_∞</i>	0.75
<i>H [m]</i>	10 665
<i>p [Pa]</i>	23 922
<i>T [K]</i>	218.9
<i>n [1/s]</i>	14.64
<i>D [m]</i>	4.2672
<i>HTR</i>	0.4
<i>κ₁ [deg]</i>	(15, 30)
<i>κ₂ [deg]</i>	(35, 50)
<i>κ₃ [deg]</i>	(0, 30)
<i>Airfoil</i>	NACA 16 series
<i>c/D [%] range at root:</i>	(16, 22)
<i>c/D [%] range at tip:</i>	(7, 15)
<i>c_{ld} range at root:</i>	(0, 0.6)
<i>c_{ld} at tip:</i>	0
<i>t/c [%] Root (SR7L):</i>	6.31%
<i>t/c [%] Tip (SR7L):</i>	2.15%

1 COLUMN WIDTH

Table 3 – Chord displacement angle κ_i ranges for the optimization presented in this paper and an additional, expanded optimization where the ranges of κ_i have been increased.

	<i>Presented optimization</i>	<i>Expanded optimization</i>
κ_1 [deg]	(15, 30)	(-45, 30)
κ_2 [deg]	(35, 50)	(-60, 50)
κ_3 [deg]	(0, 30)	(-45, 30)